



universität
wien

**Magnetostriction of
GdAg₂, PrFe₄As₁₂, and GdVO₃
measured with a Capacitance
Dilatometer**

Master Thesis

Supervisor: Dr. habil. Martin Rotter

Submitted by: Nasir Mehboob

Matrikelnummer: 0748726

Acknowledgement

I am heartily thankful to my supervisor, Dr. habil. Martin Rotter for his keen interest, encouraging discussion and friendly attitude during the course of this work. I would like to express my deepest gratitude and thanks to Ass. Prof. Dr. Herbert Müller, under the supervision of him I performed all measurements at the Technical University of Vienna.

I also want to thank Dr Piotr Wisniewski for providing sample as well as for his useful comments, and value able suggestions.

I am grateful to Dr. Mathias Doerr for helpful discussions about the magnetisation of GdAg₂ polycrystal. I would like to acknowledge Yurii Scourski and Eric for the cooperation in measurement of magnetisation of GdAg₂.

Special thank to Dr Le Tung for providing sample and taking interest in measurements. I want to thank Ismaeil Royanian for preparing the GdAg₂ sample. Thanks to univ. Prof. Bühler Paschen and her Ph D student Stephan Lauman for the technical cooperation in finding orientation of the crystal.

I am also thankful to Dr Andriy Grytsiv and Prof. Rogl for his help and cooperation in measuring a sample on the GADDS instrument.

I am grateful to Univ. Prof. Grössinger Roland who provided me opportunity to continue my Ph D under his supervision at the Technical University of Vienna.

I wish to pay my humble thanks to my affectionate parents, father in law, mother in law, brothers and sisters who remember me in their prayers.

I finally thank my wife Navida, who is also Ph D student of the University of Vienna for understanding and support.

Abstract

The magnetostriction and thermal expansion of the binary rare earth compound GdAg_2 and ternary rare earth compounds $\text{PrFe}_4\text{As}_{12}$ and GdVO_3 are investigated. A capacitance dilatometer was used for this purpose.

The thermal expansion and magnetostriction measurements of GdAg_2 were performed on a polycrystal sample and it was found that the sample was preferred oriented along [001] direction. From the standard model of rare earth magnetism the saturation magnetic field was calculated and confirmed by experiment.

The thermal expansion and magnetostriction of $\text{PrFe}_4\text{As}_{12}$ was measured on a single crystal. The magnetostriction data along and perpendicular to magnetic field cannot be explained by a random domain distribution in zero field. A microscopic model for domain distribution is presented to explain the data.

For GdVO_3 magnetostriction and thermal expansion measurements at different fields were done. The magnetic phase diagrams were constructed and compared with the phase diagram derived from X-ray and neutron diffraction measurements.

1	INTRODUCTION	5
1.1	Thermal expansion	5
1.1.1	Isotropic and anisotropic thermal expansion	5
1.2	Magnetostriction	9
1.2.1	Magnetostriction in the standard model of rare earth magnetism	10
1.2.2	The crystal field mechanism of magnetostriction	12
1.2.3	Exchange striction	13
2	EXPERIMENTAL PROCEDURE	14
2.1	Experimental methods	14
2.2	Capacitance Dilatometry	15
2.3	Calibration of the Dilatometer	18
3	RESULTS & DISCUSSIONS	29
3.1	GdAg₂	29
3.1.1	Crystal and Magnetic Structure	29
3.1.2	The magnetoelastic paradox	31
3.1.3	Magnetization	34
3.1.4	Thermal Expansion of GdAg ₂	38
3.1.5	Magnetostriction	41
3.2	PrFe₄As₁₂	45
3.2.1	Single crystal growth and structure	46
3.2.2	Thermal expansion of PrFe ₄ As ₁₂	47
3.2.3	Magnetization Study	48
3.2.4	Magnetostriction of PrFe ₄ As ₁₂	49
3.2.5	Magnetostriction along the [111] direction	53
3.3	GdVO₃	54
3.3.1	Thermal expansion along [100] direction	59
3.3.2	Magnetostriction of GdVO ₃	60
3.3.3	Discussion	62
3.3.4	Magnetostriction of GdVO ₃ along [110] direction	64

Figure 1.1 :The Crystal-field (a-c) and exchange (d-f) mechanism for magnetoelastic strain	13
Figure 2.1: Schematic drawing of the capacitance dilatometer.....	16
Figure 2.2: Detailed drawing of the miniature tilted plate capacitance dilatometer: (a) lower capacitance-plate-holder (Ag) (b) lower capacitance-plate (Ag), (c) electrical shielding of sample space (brass),(d) sample support (Ag), (e) sample, (f) isolation washer for electrical sample isolation (sapphire).(g) mounting holes, (i) plate holder nuts (brass), (j) electrical isolation (kapton), (k) disk spring (Cu–Be), (m) thread bolt (brass), (n) isolation washer for electrical isolation of capacitance plate (sapphire), (o) upper capacitance plate (Ag), (p) upper capacitance plate holder (Ag), (q) adjustment nuts, and (r) needle bearing positions (Ag).	17
Figure 2.3: Capacitance dilatometer mounted on the holder.....	18
Figure 2.4: Schematic drawing of the capacitance dilatometer. The dashed lines represent before expansion and solid lines represent after expansion.	20
Figure 2.5: This device was used to perform first measurements with the new dilatometer. With the adapted micrometer screw, it is possible to simulate the length change of a sample by simply driving a stick into the dilatometer.[2006Ale].....	26
Figure 2.6: The device from fig. 2.5 was used to test the dilatometer. A stick at the end of the micrometer screw spreads the dilatometer apart stepwise. At each point the capacitance is recorded. This is also done in the opposite direction, when the stick goes out [2006Ale].....	26
Figure 2.7: The change of the gap, which is produced in fig. 2.6, can be calculated using the capacitance change, and the formula form Eq. 2.1[2006Ale].....	26
Figure 2.8: Thermal expansion of Lead in the temperature range from 4 to 300 K compared with literature (circles).....	27
Figure 2.9: Thermal expansion of Cu in the temperature range from 4 to 300 K compared with literature (circles).....	27
Figure 2.10: Thermal expansion of Nb in the temperature range from 4 to 300 K compared with literature (circles).....	27
Figure 2.11: Thermal expansion of borosilicate in the temperature range from 4 to 300 K compared with literature (circles).....	27
Figure 3.1 Tetragonal MoSi ₂ -type structure of GdAg ₂	29
Figure 3.2 Anisotropic thermal expansion of GdAg ₂ measured by x-ray powder diffraction. The lines represent the extrapolation of the lattice contribution from the paramagnetic range by fitting Debye functions. The arrows indicate the different magnetic transition temperatures (see text).....	31
Figure 3.3 Line width of some Bragg peaks determined by X-ray powder diffraction	32
Figure 3.4 X- ray powder diffraction profile	33
Figure3.5 Temperature dependence of the reciprocal magnetic susceptibility, measured along the [001] and [110] directions in GdAg ₂ . The paramagnetic Curie temperature $\theta_p = - 52$ K is deduced from the linear extrapolation of the high temperature data. [1991Gig].....	35
Figure 3.6 Isothermal magnetization at T = 4.3 K (Pulsed field at HLD).....	35
Figure 3.7 The dotted line is the linear extrapolation of isotherm of GdAg ₂ , which meets the saturation moment of GdAu ₂ at 68 T.	36
Figure 3.8 Comparison between the thermal expansion of GdAg ₂ as measured by the dilatometer (solid curve) and by powder x-ray diffraction (from literature, points) [2007 Rot].....	39

Figure 3.9 a) & b) The varying intensities along the arcs indicate a preferred orientation.....	40
Figure 3.10 The thermal expansion of GdAg ₂	41
Figure 3.11 Derivative of thermal expansion of GdAg ₂	41
Figure 3.12 Longitudinal forced magnetostriction of textured GdAg ₂ sample at different temperatures.....	42
Figure 3.13 Perpendicular forced magnetostriction of textured GdAg ₂ sample at different temperatures.....	43
Figure 3.14 Comparison of the longitudinal (open symbols) and perpendicular (closed symbols) magnetostriction curves of the textured GdAg ₂ at temperature 4 K and 33 K.	44
Figure 3.15 Thermal expansion of GdAg ₂ parallel to applied field direction at H = 0 T, 1.5 T, and 9 T.....	45
Figure 3.16 (a) Crystal structure of skutterudite PrFe ₄ As ₁₂ (b) Three-dimensional view of unit cell in PrFe ₄ As ₁₂ [2008Hen].....	46
Figure 3.17 Thermal expansion of the PrFe ₄ As ₁₂ single crystal along the a-axis from 4 to 50 K.....	48
Figure 3.18 Derivative of relative length change with respect to temperature vs temperature.....	48
Figure 3.19 Magnetization, M, vs magnetic field, H, for different temperatures and field along the [111] (squares symbols) and [100] (circle symbols) crystallographic directions [2008Say].....	49
Figure 3.20 Transversal Magnetostriction of the PrFe ₄ As ₁₂ single crystal along [100] with magnetic field applied along [010]-direction up to 1 T at different temperatures.....	50
Figure 3.21 Longitudinal Magnetostriction of the PrFe ₄ As ₁₂ single crystal along [100] with magnetic field applied along same direction up to 1 T at different temperatures.....	51
Figure 3.22 domain distribution models to explain the magnetostriction in PrFe ₄ As ₁₂ ... (For explanation see text).....	52
Figure 3.23 longitudinal measurements of the PrFe ₄ As ₁₂ along [111] with magnetic field applied along [111] direction up to 1 T at different temperatures.....	53
Figure 3.24 Transversal magnetostrictions of the PrFe ₄ As ₁₂ along [111] with magnetic field applied perpendicular to [111] direction.....	54
Figure 3.25 (colors line): FCC, FCW magnetization of the GdVO ₃ single crystal measured at 0.1 kOe along the main axes [2006Tun].....	56
Figure 3.26 (colors online): The magnetic isotherms of the GdVO ₃ single crystal measured along the main axes at different temperatures: 1.8 K (a); 12 K (b); 50 K (c) and 110 K (d). The symbols correspond with increasing field sections, lines with decreasing sections [2006Tun].....	57
Figure 3.27 (colors) : Magnetic X-ray scattering signals obtained from the π - σ channel (a) and π - π channel (b) with the k-scan at 2.4 K. The inset in (a) shows the results of the magnetisation and the magnetostriction curves measured at 1.8 K [L. D. Tung]. .	57
Figure 3.28 (colors) Magnetic phase diagram for the Gd magnetism in a GdVO ₃ single crystal as derived from magnetic X-ray scattering. The magnetic field was applied along the a-axis, the symbols are experimental data, and the lines separating the phases are guide to the eyes. The measurements were carried out with increasing temperature [Private communication with L. D Tung].....	58
Figure 3.29 The thermal expansion of a GdVO ₃ single crystal measured along [100] direction at $\mu_0 H = 0, 0.5, 1, 1.5, 2, 2.5, 3, 4$ T.....	60
Figure 3.30 The magnetostriction of GdVO ₃ single crystal along [100] with magnetic field applied along measured direction at temperatures 2.4, 4, 5, 6.5 7 K.....	61

Figure 3.31 The magnetostriction of a GdVO_3 single crystal along $[100]$ with magnetic field applied along measured direction at temperatures 8, 9, and 10,12,14,15,16,17,20 K. 62

Figure 3.32 Magnetic phase diagram for the Gd magnetism in a GdVO_3 single crystal as derived from magnetostriction (Open symbols) and thermal expansion (Filled symbols) at different magnetic fields. The magnetic field was applied along the $[100]$ direction. The symbols are experimental data, and the lines separating the phases are guide to the eyes and derived from synchrotron data do not match exactly to present data. The measurements were carried out with increasing temperature. 63

Figure 3.33 Longitudinal magnetostriction of GdVO_3 with field applied along $[110]$ direction. 64

1 Introduction

1.1 Thermal expansion

Thermal expansion is the change in the length or in the volume of a material as its temperature is changed. It is usually expressed as a fractional change in length or volume per unit temperature change.

The coefficient of linear thermal expansion (CTE, α , or α_1) is a material property that is indicative of the extent to which a material expands upon heating. Different substances expand by different amounts. Over small temperature ranges, the thermal expansion of uniform linear objects is proportional to the temperature change.

The corresponding mathematical equation is

$$\alpha\Delta T = \frac{\Delta L}{L_o} \quad (1.1)$$

Where ΔL is the change in length of a sample, ΔT is the change in temperature, L_o is the initial length of the sample α is the linear thermal expansion coefficient.

To determine the thermal expansion coefficient, two physical quantities (displacement and temperature) must be measured on a sample that is undergoing a thermal cycle. Three of the main techniques used for CTE measurement are dilatometry, interferometry, and thermo mechanical analysis. Optical imaging can also be used at extreme temperatures. X-ray diffraction can be used to study changes in the lattice parameter but may not correspond to bulk thermal expansion.

1.1.1 Isotropic and anisotropic thermal expansion

Expansion in a material may be one of two forms: isotropic and anisotropic. In isotropic expansion, the material expands by the same extent in any direction (isotropically) upon heating. Polycrystalline aggregates and cubic materials undergo this form of expansion. In such cases, the extent of thermal expansion may be measured in terms of the volumetric thermal expansion coefficient (β), which at constant pressure P is defined as follows:

$$\beta = \frac{1}{V} \left(\frac{\partial V}{\partial T} \right)_p \quad (1.2)$$

The isotropic thermal coefficient can be expressed in terms of free energy F:

$$\beta = - \frac{\partial \ln V}{\partial P} \Big|_T \frac{\partial P}{\partial T} \Big|_V = \chi_T \frac{\partial P}{\partial T} \Big|_V = - \chi_T \frac{\partial^2 F}{\partial V \partial T} = \chi_T \frac{\partial S}{\partial T} \Big|_T \quad (1.3a)$$

With
$$\frac{1}{\chi_T} = V \frac{\partial^2 F}{\partial V^2} \quad (1.3b)$$

The temperature dependence of the isothermal compressibility χ_T is usually negligible in comparison to the volume derivative of the entropy in evaluation of Eq. 1.3a [2005Doe]. This is a good approximation for smaller temperatures. If the free energy and the entropy can be written as a sum of these contributions it is possible to do the same with β . Thus the isotropic expansion coefficient consists of different components, such as the phonon contribution, electronic contribution, and magnetic contribution. This is a good approximation if there is no coupling between the single components such as phonon-electron coupling, or if it is negligible.

$$\beta = \sum_r \beta^r = \chi_T \sum_r \left(\frac{\partial S^r}{\partial V} \right)_T \quad (1.4)$$

In Eq. 1.4 the single contributions are denoted as r in the superscript.

In anisotropic expansion, the extent of expansion will be dependent on the particular direction where the measurement is taken. To quantify anisotropic thermal expansion (e.g. in a generalised single crystal), it is more useful to define the thermal expansion in some particular crystallographic direction and in such cases, the linear expansion coefficient, α is used. This is defined as:

$$\alpha = \frac{1}{L} \left(\frac{\partial L}{\partial T} \right)_p \quad (1.5)$$

Where L is the length of the unit cell in the direction of interest. This equation may be re-written in terms of ϵ_L , the strain the direction of measurement as follows:

$$\varepsilon_L = \alpha dT \quad (1.6)$$

or, more generally, for any direction, one may use the tensorial notation:

$$\varepsilon_{ij} = \alpha_{ij} dT \quad i, j = 1, 2, 3 \quad (1.7)$$

Where ε_{ij} are the elements of the strain tensor (i.e. ε_{11} , ε_{22} and ε_{33} are the strains in the Ox_1 , Ox_2 and Ox_3 directions respectively and $\varepsilon_{12} = \varepsilon_{21}$, $\varepsilon_{13} = \varepsilon_{31}$ and $\varepsilon_{23} = \varepsilon_{32}$ are half the shear strains in the Ox_1 – Ox_2 , Ox_1 – Ox_3 and Ox_2 – Ox_3 planes respectively. It should be noted that for isotropic systems which do not experience any shear, $\alpha_{12} = \alpha_{13} = \alpha_{23} = 0$ whilst $\alpha_{11} = \alpha_{22} = \alpha_{33} = \alpha_L$. Also, in such cases, β and α_L are related through:

$$\alpha_L = \frac{\beta}{3} \quad (1.8)$$

For anisotropic systems, different values for α might exist, depending on the direction of measurement. In fact, such materials may possess positive α 's (expansion) in one direction and zero or negative α 's (contraction) in other directions.

From the Maxwell relationship, β is expressed in other form as

$$\left(\frac{\partial V}{\partial T} \right)_P = - \left(\frac{\partial S}{\partial P} \right)_T \quad (1.9)$$

Where S is the entropy of the system, from equations (1.2) and (1.9), the volumetric thermal expansion coefficient β may also be written as:

$$\beta = - \frac{1}{V} \left(\frac{\partial S}{\partial P} \right)_T \quad (1.10)$$

Also, defining the isothermal compressibility coefficient, χ_T

$$\chi_T = - \frac{1}{\kappa_T} = - \frac{1}{V} \left(\frac{\partial V}{\partial P} \right)_T \quad (1.11)$$

Where κ_T is the isothermal bulk modulus, then from equations (1.10) and (1.11):

$$\beta = \chi_T \left(\frac{\partial S}{\partial V} \right)_T = - \frac{1}{\kappa_T} \left(\frac{\partial S}{\partial V} \right)_T \quad (1.12)$$

Alternatively, using the Maxwell relationship:

$$\left(\frac{\partial P}{\partial T}\right)_V = \left(\frac{\partial S}{\partial V}\right)_T \quad (1.13)$$

then, for constant volume conditions, β may be expressed as:

$$\beta = \chi_T \left(\frac{\partial P}{\partial T}\right)_V = -\frac{1}{\kappa_T} \left(\frac{\partial P}{\partial T}\right)_V \quad (1.14)$$

An important parameter is the Grüneisen parameter γ . This parameter represents the thermal pressure from a collection of vibrating atoms and is defined as:

$$\gamma = \frac{V}{C_V} \left(\frac{\partial P}{\partial T}\right)_V \quad (1.15)$$

where C_V/V is the heat capacity per unit volume at constant volume. Thus the volumetric thermal expansion coefficient β may be written in terms of the Grüneisen parameter γ as follows:

$$\beta = \frac{\chi_T C_V}{V} \gamma = \frac{C_V}{V \kappa_T} \gamma \quad (1.16)$$

Where C_V is heat capacity at constant volume. The Grüneisen parameter is dimensionless and its sign determines whether the expansivity is positive or negative. Alternatively, for an adiabatic compression, β may be written as:

$$\beta = \frac{\chi_S C_P}{V} \gamma = \frac{C_P}{V \kappa_S} \gamma \quad (1.17)$$

Where C_p is heat capacity at constant pressure, χ_S is the adiabatic compressibility coefficient and κ_S is the adiabatic bulk modulus since these terms relate to the equivalent terms at constant temperature through:

$$\frac{\kappa_S}{\kappa_T} = \frac{\chi_T}{\chi_S} = \frac{C_P}{C_V} \quad (1.18)$$

and are defined through:

$$\beta = \frac{1}{\kappa_T} = V \left(\frac{dP}{dV}\right)_S \quad (1.19)$$

Although most materials exhibit positive thermal expansion, there are, in fact, some materials, which exhibit negative thermal expansion (NTE) in some particular temperature range. When such materials experience an increase in temperature in their NTE range, they contract (i.e. shrink in size) with the result that their density increases. NTE is generally considered to be rare, unusual and limited to certain types of structures. Nevertheless, it is important to note that NTE has been shown to take place in a very common material: water. In fact, liquid water exhibits an increase in density between when heated between 273K and 277K whilst the hexagonal form of ice has a NTE coefficient at 45K [1994 Rot].

1.2 Magnetostriction

Magnetostriction is the change of a sample's shape and dimension due to the change of its magnetic state. Magnetostriction results from the dependence of magnetic and electronic exchange interactions on interatomic distances. Magnetostriction can be observed in two ways; magnetostriction induced by an external magnetic field and the spontaneous magnetostriction which appears when the magnetic state changes with temperature. When any magnetic material is magnetized either under the influence of an applied magnetic field or it crosses an ordering temperature, its shape (anisotropic) or volume (isotropic) is changed; the measurement of this effect is called magnetostriction.

Usually the magnetostriction of solids is analysed within the framework of a phenomenological model, which takes account of the crystal symmetry [1980Cla]. Whereas this serves for practical purposes, it is not possible to derive expressions for the temperature and magnetic field dependence of the strains. For such analysis it is necessary to develop a microscopic theory of magnetoelastic effects. The most important mechanisms for the magnetostriction in rare-earth compounds are the crystal field and the exchange striction. The crystal field theory is mostly applied but recently exchange striction has been studied. However, already in the 1960s the influence of the exchange interactions on the microscopic magnetoelastic properties has been discussed for ferromagnets and cubic crystals [1968Cal, 1965Cla, 1963Cal].

1.2.1 Magnetostriction in the standard model of rare earth magnetism

The microscopic theory of magnetoelastic effects is taken from [1990Mor] and was generalized to arbitrary magnetic structures and give general expression valid for any crystal symmetry by Doerr *et. al.*[2005Doe]. We consider first order effects and assume that the magnetoelastic energy is small compared to the magnetic exchange energy. Also any dynamical couplings between the lattice and the crystal field or magnetic exchange (crystal-field-phonon and magnon-phonon interaction) are neglected and we consider only the long wavelength static limit.

The magnetic Hamiltonian for rare earth elements can be written as a sum of crystal field \mathcal{H}_{cf} , two ion exchange \mathcal{H}_{ex} , Zeeman \mathcal{H}_{ze} , and E_{el} , Parts.

$$\mathcal{H} = \mathcal{H}_{cf} + \mathcal{H}_{ex} + \mathcal{H}_{ze} + E_{el} \quad (1.20)$$

$$\mathcal{H}_{cf} = \sum_{lm,i} B_l^m(i, \bar{\varepsilon}) O_l^m(\mathbf{J}_i) \quad (1.21)$$

$$\mathcal{H}_{ex} = -\frac{1}{2} \sum_{ij\alpha\beta} \mathbf{J}_i^\alpha \mathfrak{G}_{\alpha\beta}(\bar{\varepsilon}, i-j) \mathbf{J}_j^\alpha \quad (1.22)$$

$$\mathcal{H}_{ze} = - \sum_i g_j \mu_B \mathbf{J}_i \mathbf{H} \quad (1.23)$$

The term E_{el} is the elastic energy, and thus contains all the energy contributions from the rest of the system.

The crystal field parameters B_l^m , can be determined from experiments or can be calculated from different models, the $O_l^m(\mathbf{J}_i)$ are the Stevens operators. \mathbf{J}_i is the *component* of the angular momentum operator of the ion i , and $\mathfrak{G}_{\alpha\beta}$ is the two ion interaction tensors of the Hamiltonian depend on the position of atoms in the crystal – leading to magnetoelastic interactions [1990Mor]. \mathbf{H} is the magnetic field and g_j is the Lande' factor. By these equations, and some further analysis it is possible to get an expression for the magnetostrictive strain ε_m^α . Starting point is the expansion of Eq. (1.21) and Eq. (1.22) into first order Taylor series with respect to the strain.

$$\sum_{lm,i} B_l^m(i, \bar{\varepsilon}) O_l^m(\mathbf{J}_i) \approx \sum_{lm,i} B_l^m(i, \bar{\varepsilon} = 0) O_l^m(\mathbf{J}_i) + \sum_{lm,i} \varepsilon^\alpha B_{l(\alpha)}^m(i) O_l^m(\mathbf{J}_i) + \dots \quad (124)$$

$$-\frac{1}{2} \sum_{ij} \mathbf{J}_i^\alpha \mathfrak{G}_{\alpha\beta}(ij, \bar{\epsilon}) \mathbf{J}_j^\alpha \approx -\frac{1}{2} \sum_{ij} \mathbf{J}_i^\alpha \mathfrak{G}_{\alpha\beta}(ij, \bar{\epsilon}=0) \mathbf{J}_j^\alpha - \frac{1}{2} \sum_{ij} \epsilon^\alpha \mathbf{J}_{(\alpha)}(ij) \mathbf{J} + \dots \quad (1.25)$$

$$\bar{\mathcal{J}}_{(\alpha)}(ij) = \left[\frac{\partial \bar{\mathcal{J}}(ij, \bar{\epsilon})}{\partial \epsilon^\alpha} \right]_{\epsilon=0} \quad (1.26)$$

$$B_{l(\alpha)}^m(\mathbf{i}) = \left[\frac{\partial B_l^m(\mathbf{i}, \bar{\epsilon})}{\partial \epsilon^\alpha} \right]_{\epsilon=0} \quad (1.27)$$

Usually it is sufficient to explain linear phenomena; the expansion is limited to first order in strain (harmonic approximation).

By definition the magnetic free energy is given by

$$F_m = -k_B T \ln Z \quad (1.28)$$

With the partition sum

$$Z = Tr \{ e^{-\mathcal{H}/k_B T} \} \quad (1.29)$$

Here k_B is the Boltzmann constant.

Tr is the trace of quantum mechanical operator. Inserting the Hamiltonian (1.20) into (1.28) and (1.29), calculating the derivative of the magnetic free energy F_m with respect to the strains E^α and using equation (1.22) yields the final result

$$\epsilon_m^\alpha = \epsilon_{cf}^\alpha + \epsilon_{ex}^\alpha \quad (1.30)$$

$$\epsilon_{cf}^\alpha = -\frac{1}{V} \sum_{\beta, i} s^{\alpha\beta} B_{l(\alpha)}^m(i) \langle O_l^m(\mathbf{J}_i) \rangle_{T, \mathbf{H}} \quad (1.31)$$

$$\epsilon_{ex}^\alpha = +\frac{1}{2V} \sum_{\beta, ij} s^{\alpha\beta} \langle \mathbf{J}_i \bar{\mathcal{J}}_{(\beta)}(ij) \mathbf{J}_j \rangle_{T, \mathbf{H}} \quad (1.32)$$

The magnetic contribution to the strain can be calculated as the sum of the crystal field contribution and the exchange part. From equations (1.31) and (1.32) it is clear that the whole temperature and field dependence of the magnetoelastic strain can be calculated

from thermal expectation values of the Stevens operators' equivalents $\langle O_i^m(J_i) \rangle_{T,H}$ and static correlation functions $\langle J_i^z J_j^z \rangle$ [1965Cal].

1.2.2 The crystal field mechanism of magnetostriction

The crystal field mechanism and the exchange striction can be explained more clearly by considering the simple model system shown in figure 1.1. The crystal field mechanism is shown on the left hand side of fig 1.1. The subfigure a shows two negative charges (rare earth ions) surrounded by four positive charges. The crystal field splitting Δ_{cf} of the 4f ground state is produced according to Coulomb's law. For temperature higher than the crystal field splitting Δ_{cf} of the 4f ground state multiplet the 4f charge density is spherical symmetric (figure 1.1a left) when the temperature is lower than the crystal field splitting; only the low energy crystal field states are thermally populated. This leads to a continuous deformation of the 4f charge density with decreasing temperature that leads to an increase or decrease of force between the 4f electrons and the positive charge that causes the deformation, which is called crystal field striction. A magnetostrictive strain of the crystal lattice results as indicated by the small arrows in figure 1.1a right. For this magnetostrictive effect no long-range order is necessary and it is called crystal field influence on the thermal expansion [1993Gra, 1993Gra1].

When the system orders antiferromagnetically, the shape of the 4f charge density is closely associated with magnetic anisotropy. In crystal field theory this anisotropy is governed by Stevens, factor α_J , β_J , and γ_J [1964Hut42]. For positive Stevens factor α_J (Sm³⁺, Er³⁺, Tm³⁺, Yb³⁺), the magnetic easy axis is vertical and for negative Stevens factor α_J (Ce³⁺, Pr³⁺, Nd³⁺, Tb³⁺, Dy³⁺, Ho³⁺) it will be horizontal. The magnetic moments order antiferromagnetically as indicated by large arrows in figure 1.1b for $T < T_N$. this has an influence on the distance between the positive and negative charges, and leads to spontaneous magnetostriction below T_N , as indicated by small arrows in figure 1.1. In a magnetic field normal to the magnetic moments (easy axis), the moments are turned. Due to spin orbit coupling the charge density also changes its shape and again leads to magnetostriction. Now the effect is opposite to the case described in subfigure b in figure 1.1.

1.2.3 Exchange striction

The exchange striction mechanism is shown in figure 1.1d-f. For a system with zero orbital momentum ($L=0$) the 4f charge density is spherical symmetric. There is no crystal field and the magnetostriction is dominated by the exchange striction. In such a system the direction of the magnetic moment is not determined by the crystal field but by anisotropic interactions, e.g. dipolar. The two ion interaction depends on the distance between these ions. Below the Néel temperature the exchange energy (Heisenberg, RKKY, etc.) of the system may be lowered by a change of the distance between the ions (see Fig. 1.1). A change of the distance between ions is nothing else than magnetostriction, which is referred to as exchange striction. This effect may only occur for ordered magnetic moments, which is in contrast to the crystal field mechanism. This is one possibility to separate the two mechanisms from each other. Furthermore, in systems with $L=0$ (for example Gd^{3+}) only exchange striction is possible, because the crystal field strains are zero in these systems

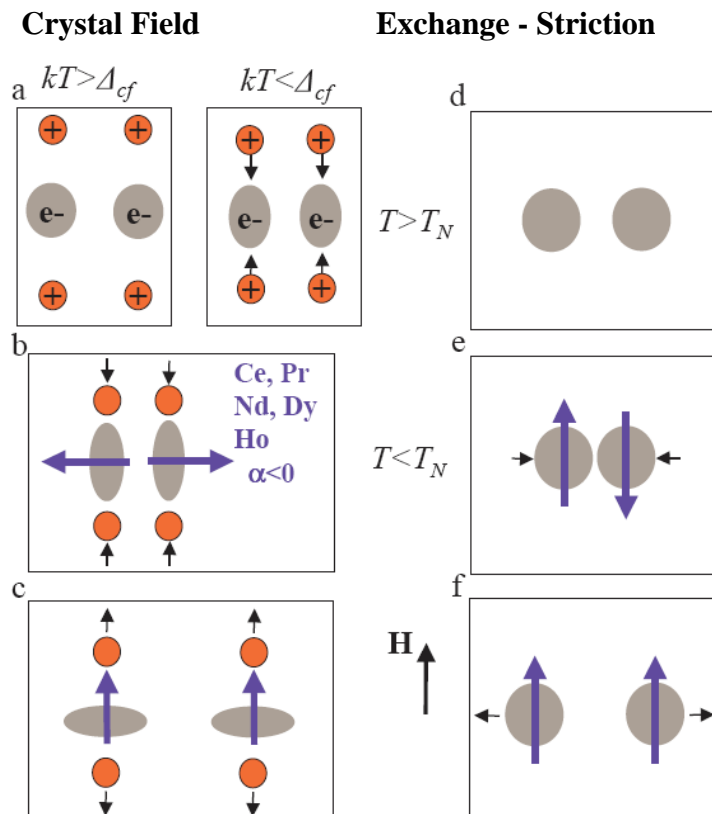


Figure 1.1 :The Crystal-field (a-c) and exchange (d-f) mechanism for magnetoelastic strain

2 Experimental Procedure

2.1 Experimental methods

Different methods are used to measure thermal expansion and magnetostriction. e.g. X-rays and neutron scattering are microscopic, strain gauges and capacitance dilatometry are macroscopic methods. All of these methods have advantages and disadvantages.

The thermal expansion and magnetostriction of solids can be determined by use of an x-ray diffractometer, i.e. measuring of the temperature and magnetic field dependence of the lattice parameter. The advantage of this 'microscopic' method is the possibility of determining the thermal expansion of the various crystallographic directions even in the case of polycrystalline samples, whereas for 'macroscopic' measurements like capacitive, optical or other methods, single crystals (in the case of noncubic materials) are necessary. The outstanding feature of the capacitance method is the high sensitivity ($\Delta l/l = 10^{-10}$), which is a few orders of magnitude better than the sensitivity of all other methods (x-ray: $\Delta l/l \approx 10^{-5}$ optical methods $\Delta l/l \approx 10^{-7}-10^{-8}$; for further comparison see [Barron *et al* (1980)]. Therefore it is possible to investigate the thermal expansion of solids at low temperatures by the capacitance method, where the relative length change $\Delta l/l$ is of order 10^{-10} .

For crystalline materials, the use of strain gauges is most simple. The strain gauge is glued on to the sample-surface. These strain gauges detect the length-change via a change in resistivity of the gauge material. One problem is that the probe has to have a flat surface, and it must be few millimetres in length in order to glue the gauge to it. The sensitivity is in the range of 1×10^{-6} running experiments from 4.2 K up to about 200 °C depending on the sensor and the glue applied.

An optical method to detect thermal and magnetic expansion is the interferometry. A change in the distance between two optical flats results in different interference pattern. They can be used to determine the value of the length change. To get an overview of the common methods refer to [2005Doe]. For the present work, all measurements were made with capacitance dilatometry proposed by M. Rotter, et al [1998Rot], which is explained in the next section.

2.2 Capacitance Dilatometry

The history of the capacitance dilatometer starts from thermal expansion measurements [1955Bij] and up to now a lot of efforts have been made (see Ref. [1998Rot] and references therein)! in order to improve its sensitivity and reproducibility.

The capacitance method is one of the most sensitive methods for measuring small length changes of solids. The basic principle of capacitance dilatometer is the change of capacitance between two capacitor plates, which can be related to a length-change of a sample. Capacitance cells with parallel plates are easy to calibrate, but usually have either big dimensions or difficulties with sample handling. Even if the problem of thermal stability of such big cells is solved, limited space in most of the magnetic coil systems causes problems, particularly when magnetostriction parallel and perpendicular ($\lambda_{||}$ and λ_{\perp}) to the field has to be measured. To minimize the cell size the capacitor design is based on the tilted plate principle [1973Bra, 1990Gen] with the sample placed in a hole in the lower capacitance plate (see Fig. 2.2), determining the maximal sample size ($3 \times 3 \times 3 \text{ mm}^3$). To obtain a reasonable accuracy the active length of the sample should be bigger than 0.5 mm. The sample can have nearly any irregular shape; only the base surface should be flat to give a stable sample position.

The tilted plate construction has a large plate area and a low volume, which gives a good sensitivity in connection with very small sensor dimensions (diameter: 20 mm, height: 14 mm). It is relatively easy to set up samples in these plates, because the plates do not have to be perfectly parallel. The schematic arrangement of the capacitance dilatometer is shown in Fig.2.1. The lower part consists of a plate holder (Ag). It includes the ring like lower capacitor plate (Ag) and the sample support (Ag). The upper part consists of the upper plate holder (Ag) and the disk like upper capacitor plate. It is separated from the lower one by two needle bearings (silver) and the sample to obtain a well-defined support on three points. Both capacitor plates as well as the sample support are insulated from the holders by sapphire washers [1983pot]. The needle bearings define an exact pivot point and avoid any transversal shift between the upper and lower plate holder.

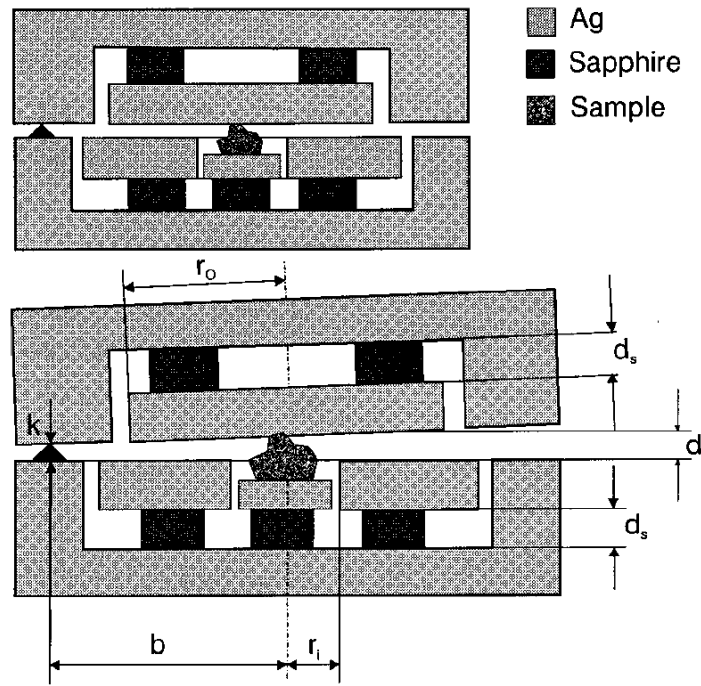


Figure 2.1: Schematic drawing of the capacitance dilatometer

Figure 2.2 shows the detailed drawing of the complete dilatometer. In addition to the schematic drawings the following parts are shown. The electrical shielding of the sample (c) is essential for screening the sample support (d) from the lower plate. The groove (l) holds the capacitance wires and ensures a good thermal contact to improve temperature stabilization. The thread bolt (m) together with the disk spring (k) fixes the position of the capacitance plate and performs the electrical connection to the plate. The disk spring fitting in the conical hole produces a well-defined force to keep the position of the capacity plate with respect to the holder. [1983pot, 1997Swe] This improved design looks much simpler than that of Pott and Schefzyk [1983pot]. The stress on the sample can be adjusted with a torque driver at the nuts (q). To obtain a good electrical insulation between plate holders [(a) and (p)] and the capacitor plates [(b) and (o)] the kapton insulation rings (j) and the Cu–Be disk springs (k) must be aligned exactly and fit precisely in the holes. (h) is the temperature sensor platform.

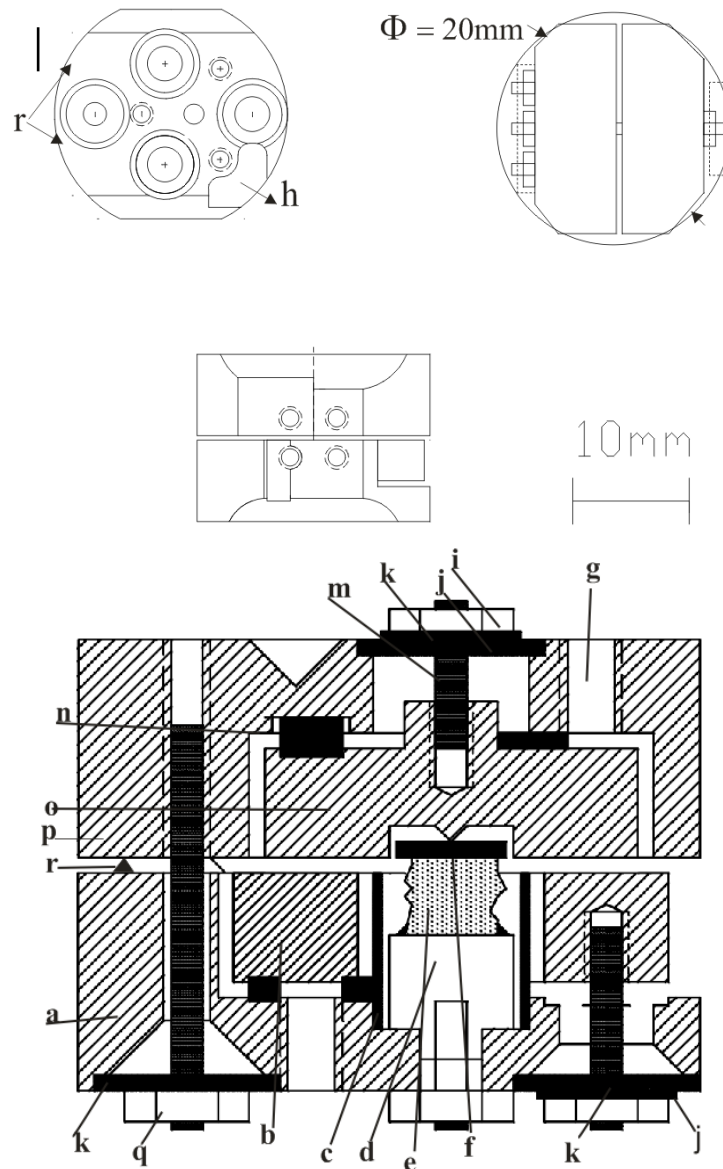


Figure 2.2: Detailed drawing of the miniature tilted plate capacitance dilatometer: (a) lower capacitance-plate-holder (Ag) (b) lower capacitance-plate (Ag), (c) electrical shielding of sample space (brass), (d) sample support (Ag), (e) sample, (f) isolation washer for electrical sample isolation (sapphire). (g) mounting holes, (i) plate holder nuts (brass), (j) electrical isolation (kapton), (k) disk spring (Cu-Be), (m) thread bolt (brass), (n) isolation washer for electrical isolation of capacitance plate (sapphire), (o) upper capacitance plate (Ag), (p) upper capacitance plate holder (Ag), (q) adjustment nuts, and (r) needle bearing positions (Ag).

Figure 2.3 shows the two views of assembled dilatometer is mounted on the holder in the desired setup. The wires for the measurement are soldered at the dilatometer holder, and have to be soldered to the threaded bolts, that connect the wires to the capacitance plates.

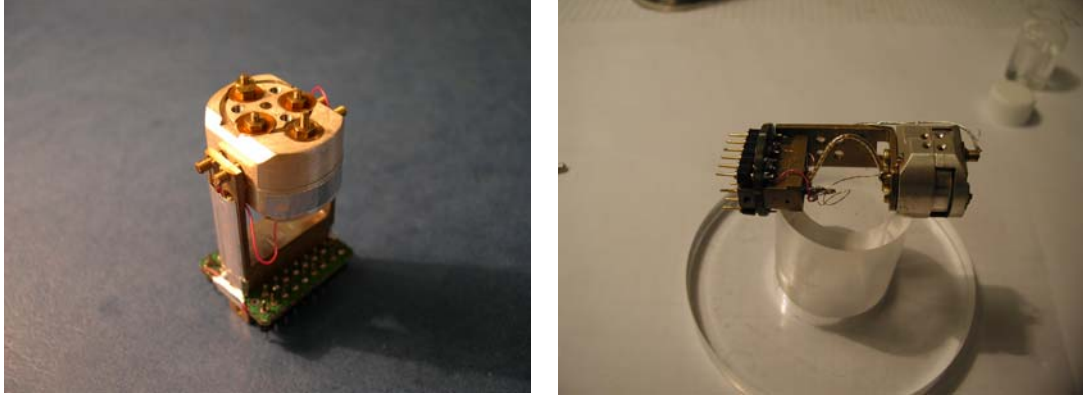


Figure 2.3: Capacitance dilatometer mounted on the holder.

2.3 Calibration of the Dilatometer

Tilted dilatometers have the big advantage in that they are much easier to set up than normal parallel dilatometers; however a numerical calibration to calculate the sample length is needed. For the tilted dilatometers, the gap $d(T)$ has to be numerically determined by

$$d(T) = \frac{2\varepsilon_o}{C(T)} \left[A_o(T) \frac{1 - \sqrt{1 - \gamma_o^2}}{\gamma_o^2} - A_i(T) \frac{1 - \sqrt{1 - \gamma_i^2}}{\gamma_i^2} \right] \quad (2.1)$$

where ε_o is the electric constant, $C(T)$ is the capacitor A_o and A_i are the area of the outer and inner capacitor plate, and γ is the quantity determined by the angle of the tilted plates [1998Rot].

With

$$\gamma_o = \frac{r_o}{b} \left[\frac{k(T)}{d(T)} - 1 \right] \quad (2.2)$$

$$\gamma_i = \frac{r_i}{b} \left[\frac{k(T)}{d(T)} - 1 \right] \quad (2.3)$$

Where r_o is the outer plate radius, r_i is the inner plate radius, b is the distance between center of capacitor and pivot (see figure 2.1).

$$k(T) = k(T_o) \left[1 + \frac{\Delta l_{Ag-Lit}}{l}(T) \right] \quad (2.4)$$

Where $k(T_o)$ is the pivot distance at $T_o = 300$ K, d_s the thickness of sapphire washers (0.8 mm), $(\Delta l_{Ag-Lit}/l)(T)$ is the thermal expansion of Ag from literature, [1972Whi] and $(\Delta l_{sapphire}/l)(T)$ the thermal expansion of sapphire from literature[1993Whi].

To determine the pivot distance $k(T_o)$ the plates have to be adjusted parallel (using the calibration mount) and the corresponding capacitance C_o has to be measured.

The temperature dependence of the inner plate $A_i = r_i^2 \pi$ is given by.

$$A_i(T) = A_i(T_o) \left[1 + \frac{\Delta l_{Ag-Lit}}{l}(T) \right]^2 \quad (2.5)$$

Similar, A_o is the outer capacitance area $r_o^2 \pi$ with temperature dependence.

$$A_o(T) = A_o(T_o) \left[1 + \frac{\Delta l_{Ag-Lit}}{l}(T) \right]^2 \quad (2.6)$$

The terms in the square brackets in Eq (2.5) and (2.6) stand for the linear thermal expansion of Ag. This expansion changes the area of the capacitor plates, and therefore the capacitance.

Once $d(T)$ is obtained as a function of the temperature, the thermal expansion of the sample in question $\frac{\Delta l_{Sample}}{l}(T)$ is calculated from geometrical considerations shown in

figure 2.4

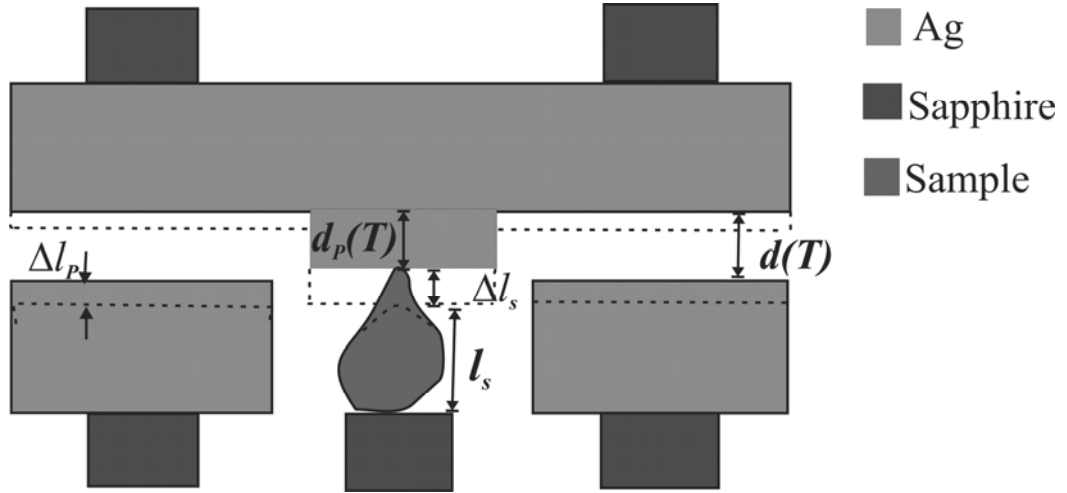


Figure 2.4: Schematic drawing of the capacitance dilatometer. The dashed lines represent before expansion and solid lines represent after expansion.

For simplicity we show a parallel plate configuration: it is essentially a cut normal to that shown in figure 2.1 and 2.2. Introducing the tilt will not change the formulas derived from this scheme. To ease the formula derivation, the sapphire isolation washer (SW) is placed below the sample.

From figure (2.4) we have following equation

$$d(T) + \Delta l_p = \Delta l_{Sample} + d_p(T) \quad (2.7)$$

Where Δl_p and Δl_{Sample} are change in length of capacitance plates (Ag) and Sample respectively, which are given as

$$\Delta l_p = \frac{\Delta l_{Ag-Lit}(T)}{l} l_s \quad (2.8a)$$

$$\Delta l_{Sample} = \frac{\Delta l_{Sample}(T)}{l} l_s \quad (2.8b)$$

$d(T)$ is the gap between capacitance plates at temperature T and $d_p(T)$ is the thickness of spacer at temperature T , and is given as

$$d_p(T) = d(T_o) \left(1 + \frac{\Delta l_{Ag-lit}(T)}{l} \right) \quad (2.9)$$

Where $d(T_o)$ is the gap between the capacitance plates at a temperature T_o .

Substituting values from equations (2.8) and (2.9) in equation (2.7)

$$d(T) + \frac{\Delta l_{Ag-lit}(T)l_s}{l} = \frac{\Delta l_{Sample}(T)l_s}{l} + d(T_o) \left(1 + \frac{\Delta l_{Ag-lit}(T)}{l} \right) \quad (2.10)$$

By rearranging

$$d(T) - d(T_o) + \frac{\Delta l_{Ag-lit}(T)l_s}{l} = \frac{\Delta l_{Sample}(T)l_s}{l} + d(T_o) \frac{\Delta l_{Ag-lit}(T)}{l} \quad (2.11)$$

In order to eliminate all influences of the expansion of silver we introduce the new definitions that is the normalized gap $\hat{d}(T)$ and the normalized area of outer and inner capacitor plates $\hat{A}_o(T)$ and $\hat{A}_i(T)$.

$$\hat{d}(T) \equiv \frac{d(T)}{1 + \frac{\Delta l_{Ag-lit}(T)}{l}} \quad (2.10a)$$

Implying
$$d(T) \equiv \hat{d}(T) \left(1 + \frac{\Delta l_{Ag-lit}(T)}{l} \right)$$

Inserting (2.10a) into (2.5) and (2.6) the area of outer and inner capacitor plates become

$$\hat{A}_o(T) \equiv \frac{A_o(T)}{1 + \frac{\Delta l_{Ag-lit}(T)}{l}} = A_o(T_o) \left(1 + \frac{\Delta l_{Ag-Lit}(T)}{l} \right) \quad (2.10b)$$

$$\hat{A}_i(T) = \frac{A_i(T)}{1 + \frac{\Delta l_{Ag-lit}(T)}{l}} = A_i(T_o) \left(1 + \frac{\Delta l_{Ag-Lit}(T)}{l} \right) \quad (2.10c)$$

and at $T=T_o$ $d(T_o) = \hat{d}(T_o)$

By applying these new definitions equation (2.11) becomes

$$\hat{d}(T) \left(1 + \frac{\Delta l_{Ag-lit}}{l} \right) (T) - \hat{d}(T_o) + \frac{\Delta l_{Ag-lit}}{l} (T) l_s = \frac{\Delta l_{Sample}}{l} (T) l_s + \hat{d}(T_o) \frac{\Delta l_{Ag-lit}}{l} (T) \quad (2.11a)$$

Rearranging gives

$$\frac{\hat{d}(T) - \hat{d}(T_o)}{l_s} + \frac{\hat{d}(T) - \hat{d}(T_o)}{l_s} \frac{\Delta l_{Ag-lit}}{l} (T) + \frac{\Delta l_{Ag-lit}}{l} (T) = \frac{\Delta l_{Sample}}{l} (T) \quad (2.12)$$

Let $\Delta \hat{d}_s(T) \equiv \hat{d}(T) - \hat{d}(T_o)$

$$\frac{\Delta l_{Sample}}{l} (T) = \frac{\Delta \hat{d}_s(T)}{l_s} + \left(\frac{\Delta \hat{d}_s(T)}{l_s} \right) \frac{\Delta l_{Ag-lit}}{l} (T) + \frac{\Delta l_{Ag-lit}}{l} (T) \quad (2.13)$$

By simplifying we get

$$\frac{\Delta l_{Sample}}{l} (T) = \frac{\Delta \hat{d}_s(T)}{l_s} \left(1 + \frac{\Delta l_{Ag-lit}}{l} \right) (T) + \frac{\Delta l_{Ag-lit}}{l} (T) \quad (2.14)$$

Equation (2.14) is the required equation for calculating the thermal expansion of the sample.

Therefore we rewrite equations (2.1)-(2.6) in terms of $\hat{d}(T)$. We have the new set of equations used for data evaluation.

$$\hat{d}(T) = \frac{2\varepsilon_o}{C(T)} \left[\hat{A}_o(T) \frac{I - \sqrt{I - \gamma_o^2}}{\gamma_o^2} - \hat{A}_i(T) \frac{I - \sqrt{I - \gamma_i^2}}{\gamma_i^2} \right] \quad (2.14a)$$

$$\gamma_o = \frac{r_o}{b} \left[\frac{k(T_o)}{\hat{d}(T)} - I \right] \quad (2.14b)$$

$$\gamma_i = \frac{r_i}{b} \left[\frac{k(T_o)}{\hat{d}(T)} - I \right] \quad (2.14c)$$

$$\hat{A}_i(T) = \pi r_i^2 \left[I + \frac{\Delta l_{Ag-lit}(T)}{l} \right] \quad (2.14d)$$

$$\hat{A}_o(T) = \pi r_o^2 \left[I + \frac{\Delta l_{Ag-lit}(T)}{l} \right] \quad (2.14e)$$

Where $\hat{d}(T)$, $\hat{A}_i(T)$ and $\hat{A}_o(T)$ are defined in equations (2.10a) and (2.10b).

Since r_i , r_o , $k(T_o)$ and $\frac{\Delta l_{Ag-lit}(T)}{l}$ are all known, by using these values in eqn 2.14a-

2.14e we can find $\hat{d}(T)$.

Once $\hat{d}(T)$ is obtained as a function of the temperature, the thermal expansion of the sample in question $\frac{\Delta l_{Sample}(T)}{l}$ is calculated by using equation (2.14).

Let us assume a piece of silver is used as a sample then thermal expansion of silver sample must agree with literature data that is

$$\frac{\Delta l_{Ag-lit}(T)}{l} = \frac{\Delta l_{Sample}(T)}{l} \quad (2.15)$$

Then from equation (2.14) we have

$$\Delta \hat{d}_s(T) = 0 \quad (2.15a)$$

However in reality we measure $\Delta \hat{d}_s(T) \neq 0$ because the silver of the dilatometer is not pure and also the imperfection of the dilatometer more over the silver plates of capacitor is also not hundred percent silver so Ag sample and Ag capacitance plates do not expand or contract with same ratio. Therefore the resulting change of the gap is not zero. In order to compensate for these dilatometer effects, the zero signal is subtracted from the sample signal in the data evaluation; Therefore equation (2.14) can be written as

$$\frac{\Delta l_{Sample}(T)}{l} = \left(\frac{\Delta \hat{d}_{Sample}(T)}{l_s} - \frac{\Delta \hat{d}_{Ag-Sample}(T)}{l_s} \right) \left(1 + \frac{\Delta l_{Ag-lit}(T)}{l} \right) + \frac{\Delta l_{Ag-lit}(T)}{l} \quad (2.16)$$

Where $\Delta \hat{d}_{Sample} = \hat{d}_{Sample}(T) - \hat{d}_{Sample}(T_0)$ is the measurement of the sample, and $\Delta d_{Ag-Sample}(T)$ is the measurement of an Ag for reference (calibration sample).

Note that usually $\Delta \hat{d} \ll l_s$, therefore in (2.15) the second term on the right hand side can be approximately

$$\left(1 + \frac{\Delta l_{Ag-lit}(T)}{l} \right) \approx 1$$

We get

$$\frac{\Delta l_{Sample}(T)}{l} = \frac{\Delta \hat{d}_{Sample}(T)}{l_s} - \frac{\Delta \hat{d}_{Ag-Sample}(T)}{l_s} + \frac{\Delta l_{Ag-lit}(T)}{l} \quad (2.17)$$

For a new built dilatometer it is necessary to perform some consistency checks and measurements. In the first step the correct working of the dilatometer was tested without any sample by simply moving the capacitance plates away from each other with a special device shown in Fig. 2.5. The part with the nonius is kept and the counter part is not used. On the front end of the screw there is a stick with a tip mounted. This part of the micrometer screw is surrounded by brass plates. The dilatometer can be mounted on the front brass plate from upper capacitance plate housing side. In the upper part of the dilatometer housing there is a hole through which the tip of the micrometer screw can penetrate. The tip goes inside the dilatometer until it touches the other half of the dilatometer. If the stick is screwed further inside, it forces the halves apart.

Now with this arrangement it is easy to check if the forced gap between the dilatometer halves agrees with the calculated gap. Screw the micrometer, which pushes the thin rod with in the device. The tip is pushed inside the hole on the upper housing of the dilatometer with a certain step width by the micrometer screw. The capacitance is measured with the capacitance-bridge, and saved to a file. This gives the data shown in Fig. 2.7. The software calculates then the gap between the plates with the formulas in Eqs. 2.1 to 2.6. These values are stored to a file. Then both values, namely the forced gap and the calculated gap, can be compared. They are shown in Fig. 2.7. The x-axis is the distance that is was measured with the micrometer screw, and the y-axis is the calculated gap. The dotted line accords to the measured points and the continuous line is a 45° line. The total length-change was 0.295 mm, which is rather large compared to the length-changes measured at typical thermal expansion, or magnetostriction experiments.

The performance of dilatometer is also verified by some standard materials having large expansion and small expansion. For example Lead is the softest material and therefore shows the largest expansion. In a temperature range of approximately 300 K, the relative length change is approximately 7×10^{-3} . Expansion of Copper is (3×10^{-3}) in same temperature range. The element with the least expansion is borosilicate with a relative length change of 8×10^{-4} . This is a factor ten less, than Pb. Please note that in case of extremely low expansion materials a small temperature measurement error can have a large effect on the final signal.

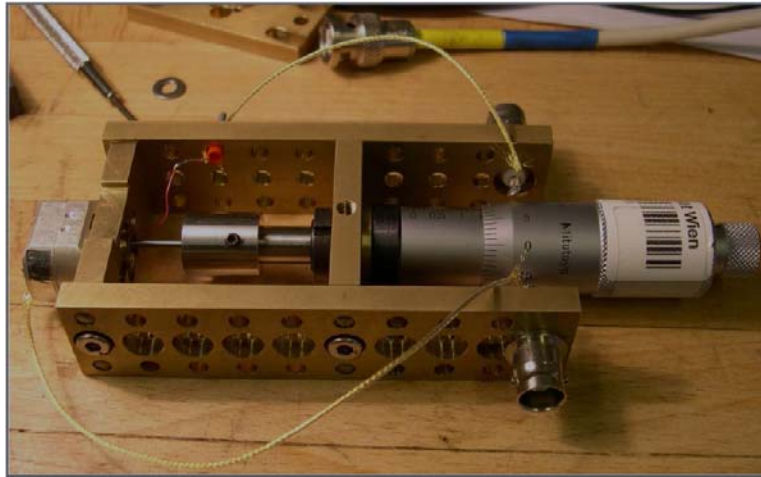


Figure 2.5: This device was used to perform first measurements with the new dilatometer. With the adapted micrometer screw, it is possible to simulate the length change of a sample by simply driving a stick into the dilatometer.[2006Ale]

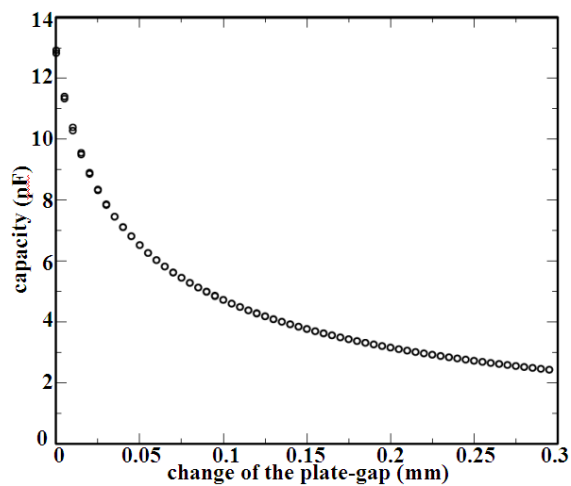


Figure 2.6: The device from fig. 2.5 was used to test the dilatometer. A stick at the end of the micrometer screw spreads the dilatometer apart stepwise. At each point the capacitance is recorded. This is also done in the opposite direction, when the stick goes out [2006Ale].

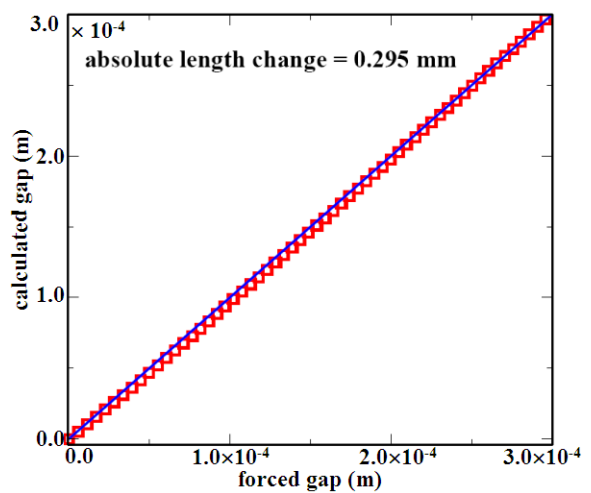


Figure 2.7: The change of the gap, which is produced in fig. 2.6, can be calculated using the capacitance change, and the formula from Eq. 2.1[2006Ale].

The dilatometer works better with materials that show large thermal expansion. The error between data in literature and experiment with this dilatometer is less than 1% in the case of Pb, and Cu. This relative error gets larger when low expansion materials such as Nb, and and borosilicate are measured.

Figures 2.7 to 2.11 show the thermal expansion of the selected materials. All data is compared with literature [1977The]. Circles indicate the values from literature.

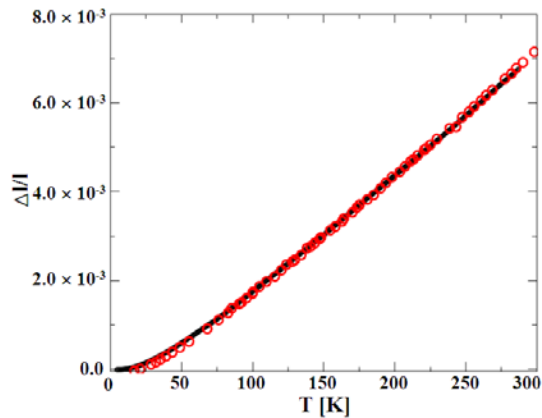


Figure 2.8: Thermal expansion of Lead in the temperature range from 4 to 300 K compared with literature (circles).

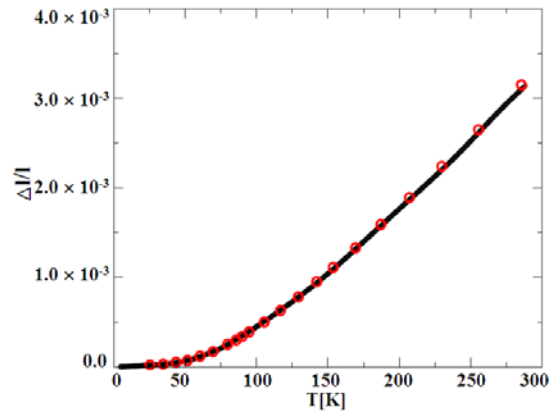


Figure 2.9: Thermal expansion of Cu in the temperature range from 4 to 300 K compared with literature (circles).

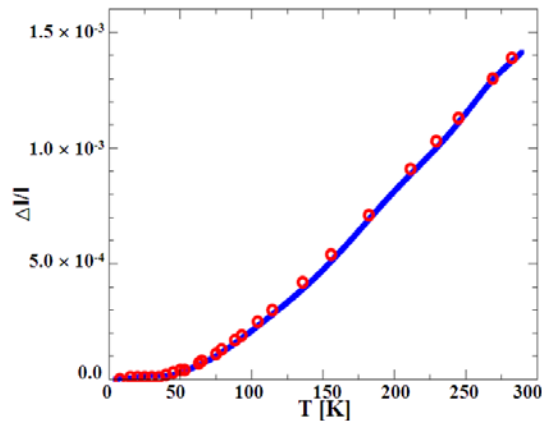


Figure 2.10: Thermal expansion of Nb in the temperature range from 4 to 300 K compared with literature (circles).

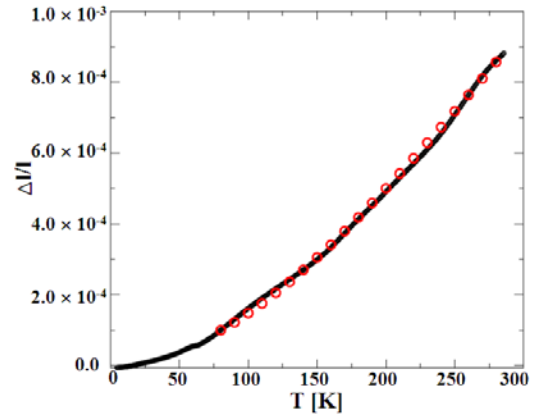


Figure 2.11: Thermal expansion of borosilicate in the temperature range from 4 to 300 K compared with literature (circles).

Sources of error

One can come across by following problems while handling dilatometer

- If a contact of sample is not in the centre of the capacitance plates (that it is offset position left or right by Δx). This produces an error in capacitance gap as result in capacity of capacitor. Then the error in measuring sample could be

$$\Delta d_{meas} = \left(1 + \frac{\Delta x}{b}\right) \Delta d_{real}$$

Where b is the distance between centre of capacitor and pivot (see Fig 2.1)

- If there is a temperature measurement error dT then from eq 2.16 the measurement error in the length of sample if sample is different from Ag is.

$$d\left(\frac{\Delta l_s}{l}(T)\right) = \left(d\frac{\frac{\Delta l_s}{l}}{dT}(T)\right) dT \cong \frac{1}{l} \frac{d}{dT} \Delta \hat{d}_s dT = d\left(\frac{\Delta \hat{d}_s}{l}\right)$$

In case of extremely low expansion materials, a small temperature measurement error can have a large effect on the final signal (i.e. the error in $\Delta l_s/l$ is related to the temperature error in $\Delta \hat{d}_s/l$, which may be bigger than $\Delta l_s/l$).

- Tilt of sample due to torque by magnetic field: If a sample has big mass, size and particularly having large anisotropy it may be turned by the applied magnetic field due to a large torque (moment). Therefore one cannot measure the magnetostriction along a particular direction, so the size and mass of such sample must kept small.
- If the size and the mass of the sample is very small and also a sample is in the form of strip one have to glue it on the holder for measurement but there is a problem during the magnetic field applied, the field may produce hump in the center of the sample because of shear stress and non-uniform strain in the sample.

These are the problems one can face in selecting the size of the sample. Therefore the size and mass of sample must be carefully selected to avoid error.

3 Results & Discussions

3.1 GdAg₂

3.1.1 Crystal and Magnetic Structure

GdAg₂ is a heavy rare earth compound that crystallizes in the tetragonal MoSi₂-type structure [1967 Dwi]. The space group is $I 4/mmm$ with Gd on the 2a sites (point symmetry $4/mmm$) and Ag on the 4e sites. This structure can roughly be viewed as being composed of three tetragonally distorted body centered cubes along c-direction ($a = 0.3716$ nm, $c = 0.926$ nm).

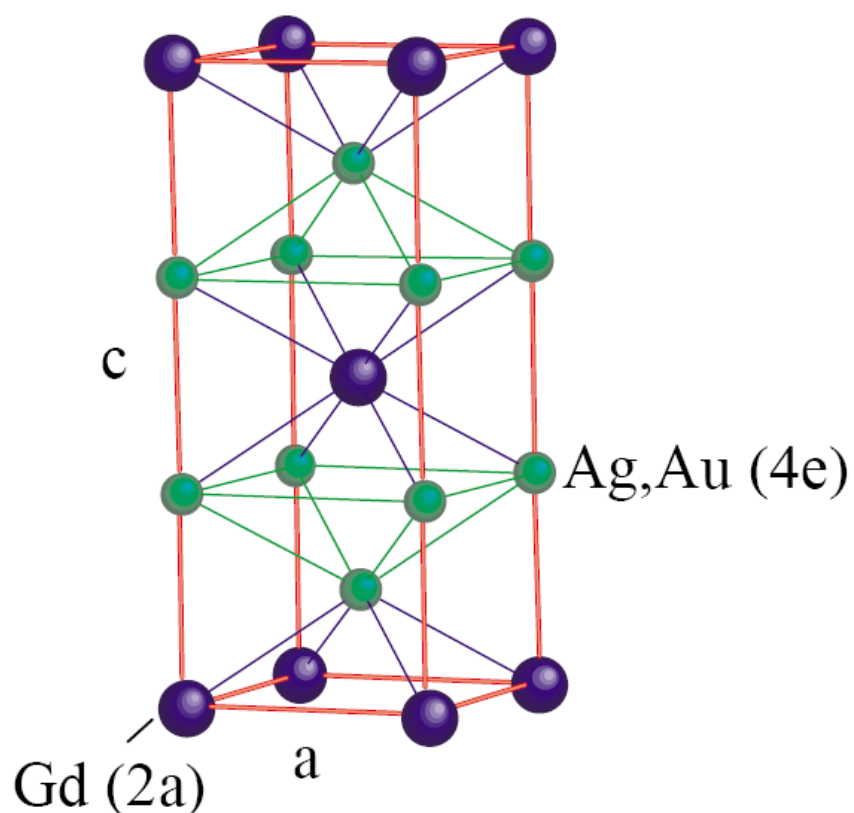


Figure 3.1 Tetragonal MoSi₂-type structure of GdAg₂

The z atomic position parameter of the 4e sites (point symmetry $4mm$) is about 1/3 and a value of $z_{Ag} = 0.327 \pm 0.004$ has been determined from neutron diffraction experiments [1991Gig].

From resistivity measurements GdAg₂ has first been reported to order magnetically at about 27 K [1975Ohas]. Further studies [1991Gig, 2002Lin] including specific heat, resistivity, thermal expansion and magnetization measurements as well as first neutron powder diffraction experiments, showed that this compound orders antiferromagnetically below $T_N \approx 22.7$ K with two further first-order magnetic transitions at $T_{R1} \approx 21.2$ K and $T_{R2} \approx 10.8$ K. The observed first-order magnetic transitions in the ordered range have been attributed to anisotropic terms in the two-ion Gd-Gd exchange interaction. A further peculiarity, also mentioned by [Gig (1991)] is that the magnetic ordering temperature of GdAg₂ is lower than in TbAg₂ ($T_N = 34.8$ K), according to De Gennes the critical temperature is proportional to the de Gennes factor $DG = (g-1)^2 J(J+1)$, (where g is the Landé factor and J is the total angular momentum of R^{+3} Hund's rule ground state) provided that the susceptibility of the conduction electron gas is constant [1991Jen]. This relationship is accurately obeyed by most of heavy rare earths. Since for Gd the de Gennes factor is $DG = 15.75$ and for Tb $DG = 10.50$ [1991Jen], i.e. the de Gennes factor for Gd is higher than for Tb, so its ordering temperature should be higher but GdAg₂ violates the De Gennes law. This has been referred to a change in the conduction band due to the boundary situation of GdAg₂ concerning the crystal structure, i.e. only the RAg₂ with heavy R, starting from Gd, show the MoSi₂ type of structure. Fig. 3.2 shows the temperature dependence of the lattice parameters as well as of the volume of GdAg₂ measured by low temperature x-ray diffraction. As can be seen there is a pronounced spontaneous anisotropic magnetostriction effect due to the magnetic ordering with no significant change at T_{R2} . An estimation of the magnetic contribution to the thermal expansion by extrapolating from the paramagnetic range down to 0 K gives the values $(\Delta a/a)_{mag} \approx 0.38 \times 10^{-3}$ and $(\Delta c/c)_{mag} \approx -0.6 \times 10^{-3}$. This leads to a clearly visible magnetically induced change of the c/a ratio of $(\Delta(c/a)/(c/a))_{mag} \approx -0.9 \times 10^{-3}$ but to no measurable volume magnetostriction within the sensitivity of the x-ray experiment $[|(\Delta V/V)_{mag}| < 0.1 \times 10^{-3}]$ [2002Lin].

GdAu₂ and GdAg₂ are isostructural compounds (Figure 3.1). GdAu₂ orders antiferromagnetically like GdAg₂ but at a much higher ordering temperature of $T_N = 50$ K [1996Tun]. Unlike GdAg₂ there is no measurable spontaneous magnetoelastic effect at all.

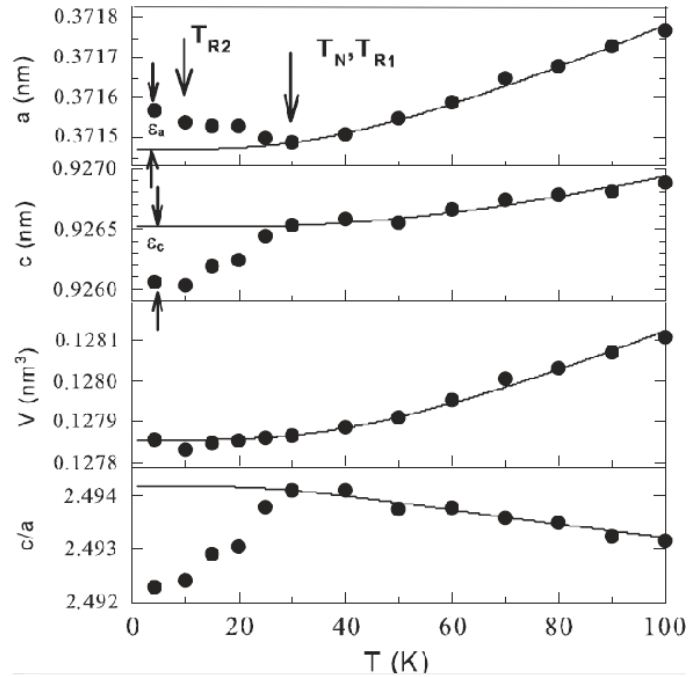


Figure 3.2 Anisotropic thermal expansion of GdAg_2 measured by x-ray powder diffraction. The lines represent the extrapolation of the lattice contribution from the paramagnetic range by fitting Debye functions. The arrows indicate the different magnetic transition temperatures (see text).

3.1.2 The magnetoelastic paradox

The magnetoelastic paradox means that in antiferromagnetic systems without orbital moment ($L = 0$) symmetry-breaking distortions below the Néel temperature are expected, but have not been found. The experimental evidence of magnetoelastic paradox in GdAg_2 is given by M. Rotter *et al.*[2006Rot]

Current theories [2005Doe] on the microscopic mechanism of magnetostriction are based on two effects—the strain dependence of the magnetic anisotropy and the strain dependence of the exchange interaction. For isotropic systems the only source of magnetostriction is believed to be exchange striction (ES). According to the ES model a symmetry breaking lattice distortion is not possible for ferromagnetic (fm) order, but should be associated with antiferromagnetic (afm) order. But experimentally such symmetry-breaking lattice distortions have not been found in isotropic systems based on the largest spin moment for instance Gd^{3+} -based compounds ($S = 7/2$, $L = 0$). This

discrepancy between the results of the ES model and experimental data is called magnetoelastic paradox (MEP) [2006Rot].

Figure 3.3 provides the experimental evidence of the magnetoelastic paradox in GdAg₂. Comparison between the line width of some X-ray reflections of GdAg₂ above and below the Néel temperature ($T_N = 22.7$ K) to the temperature dependence of the lattice parameters shows a spontaneous magnetostriction of the order of $\varepsilon_a, \varepsilon_c = \pm 3 \times 10^{-4}$ associated with the afm order (see fig 3.2). This strain conserves the tetragonal symmetry and the volume, only the c/a ratio is changed drastically (figure 3.2). The afm propagation vector has been estimated from hot neutron powder diffraction $(\frac{1}{4} \frac{2}{3} 0)$ [2007Rot] and a distortion of the crystal along this direction should appear according to the ES model thus breaking the tetragonal symmetry of the lattice. This distortion should be in magnitude similar to the spontaneous magnetostrictive symmetry conserving strain of the lattice parameters. From a strain of $\varepsilon = 3 \times 10^{-4}$ a line broadening of the reflections in the order of 0.1° is expected. No such line broadening can be seen in the powder X-ray diffraction data of GdAg₂ (Fig. 3.3) in contrast to this prediction of the ES model.

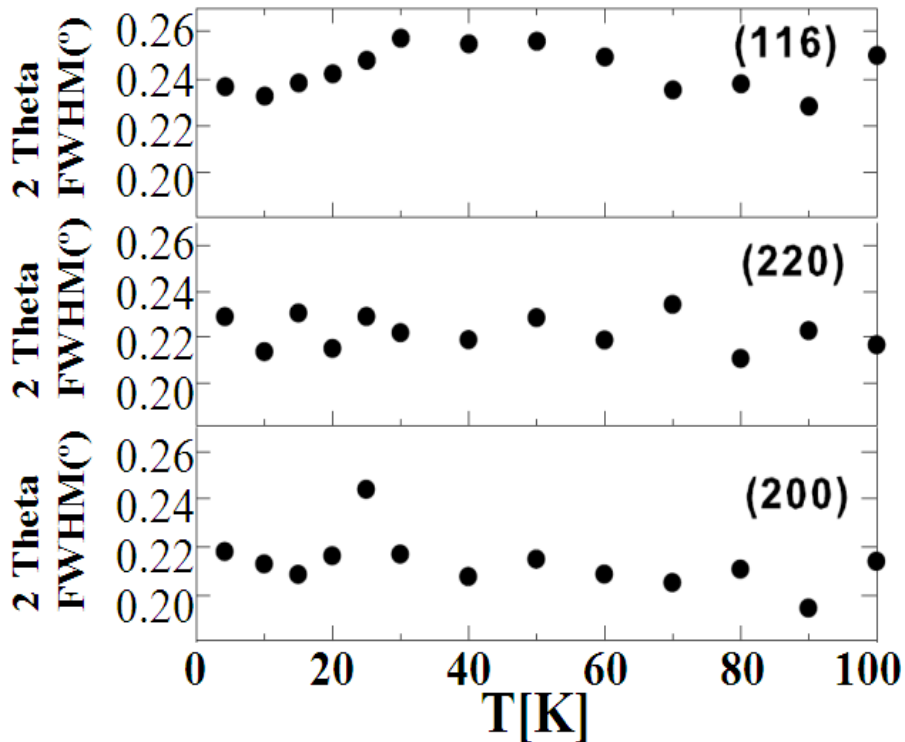


Figure 3.3 Line width of some Bragg peaks determined by X-ray powder diffraction

In the present work we carried out linear thermal expansion ($\Delta L/L$) and magnetostriction at selected temperatures with the magnetic field parallel and perpendicular to the measuring direction on the polycrystalline GdAg_2 sample.

The linear thermal expansion and magnetostriction were performed at the Technical University Vienna in collaboration with Dr Herbert Müller. For this measurement, a high-accuracy miniature capacitance dilatometer was used. The linear thermal expansion in absence of magnetic field was measured in 4 K — 290 K range and forced magnetostriction up to 9 T.

The sample of GdAg_2 was prepared by melting directly pure metals Gd and Ag in arc furnace on copper hearth. Titanium was used as getter. Grinding served to remove the oxidized layer from the surface cleaned Gd. The sample was then sealed in an evacuated quartz tube and annealed at 850°C for 4 days. The sample was analyzed by x-ray powder diffraction with a Guinier-Huber image plate system ($\text{Cu-K}\alpha_1$; $8^\circ < 2\theta < 100^\circ$) at Institute of Physical Chemistry, University of Vienna, and was found to be almost single phase with traces of impurities, probably some oxides (Fig 3.4). The sample was cut in size of approximately (2x1.84x1.78) mm. The sample is not sensitive to air so there is no need to protect it from air.

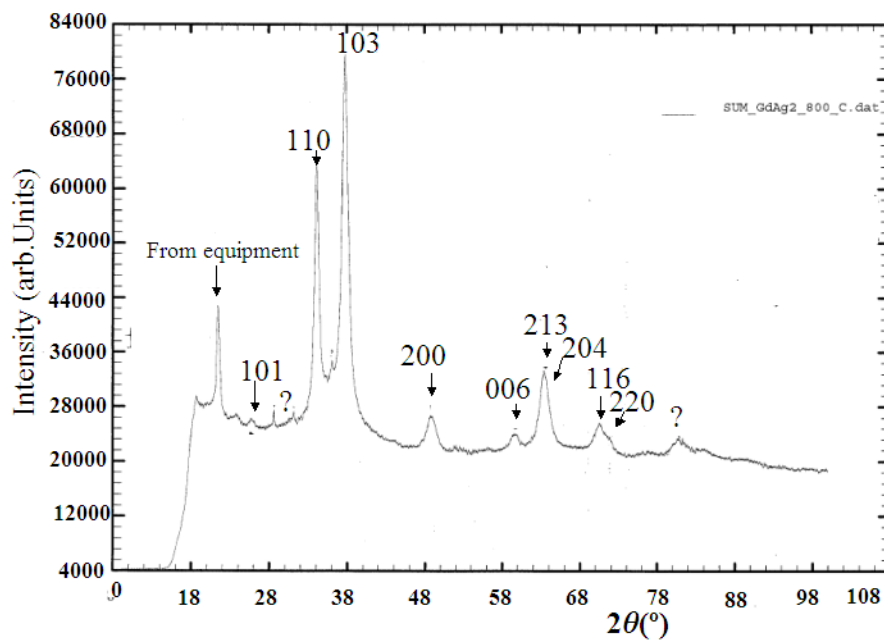


Figure 3.4 X- ray powder diffraction profile

3.1.3 Magnetization

Data from literature shown in figure 3.5 shows that the susceptibility is perfectly isotropic between the [001] axis and the [110] direction in the basal plane. Bilinear interactions are negative leading to a paramagnetic Curie temperature $\Theta_p = -52$ K. the paramagnetic moment is $8.49 \mu_B$, instead of the free ion value $7.94\mu_B$ [1991Gig]. Which is calculated theoretically by $Gd = 2[j(j+1)]^{1/2}$, $s = j = 3.5$. This error may be due to contribution of 5d electron or may be Ag contribution or it may be experimental error.

Figure 3.6 shows the graph of pulse field magnetization of $GdAg_2$ as a function of magnetic field $\mu_0 H$. The magnetization of $GdAg_2$ polycrystal was measured in the Hochfeld-Magnetlabor Dresden (HLD). The saturation field was found 37 T. However, this value is in contrast to former magnetization measurements of $GdAu_2$ and $GdAg_2$ polycrystals as a function of magnetic field $\mu_0 H$ at the High Magnet Field Lab at the St. Radbound University of Nijmegen (The Netherlands) by cantilever magnetometer in steady field [private communication] This data are shown in Figure 3.7. The isotherms are linear and the saturation magnetization M_s for $GdAu_2$ was observed $6.8\mu_B/Gd$ at magnetic field $H_s = 28$ T. There was no magnetic transition observed up to 33 T for $GdAg_2$. Since $GdAu_2$ and $GdAg_2$ are, isostructural compounds the saturation magnetic field for $GdAg_2$ can be predicted by the linear extrapolation of isotherm of $GdAg_2$, which meets the saturation moment at 68 T. Therefore, the saturation magnetic field supposed to be approximately 68 T from the cantilever magnetisation measurements in steady fields. It will be shown below, that this value is much higher than expected from theory. Moreover, it is also much higher than the value observed in the pulsed field measurements. Possible explanations for this unusual result are: In the magnetization measurement at HFML Nijmegen a very thin piece of $GdAg_2$ textured polycrystal was used and it could be that this piece was oriented more or less in hard direction.

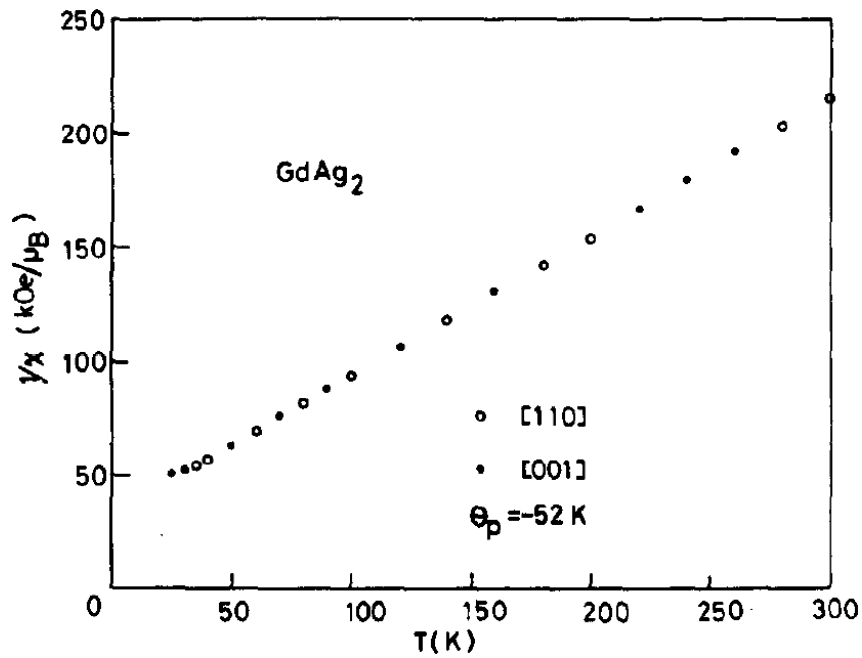


Figure 3.5 Temperature dependence of the reciprocal magnetic susceptibility, measured along the [001] and [110] directions in GdAg₂. The paramagnetic Curie temperature $\theta_p = -52$ K is deduced from the linear extrapolation of the high temperature data. [1991Gig].

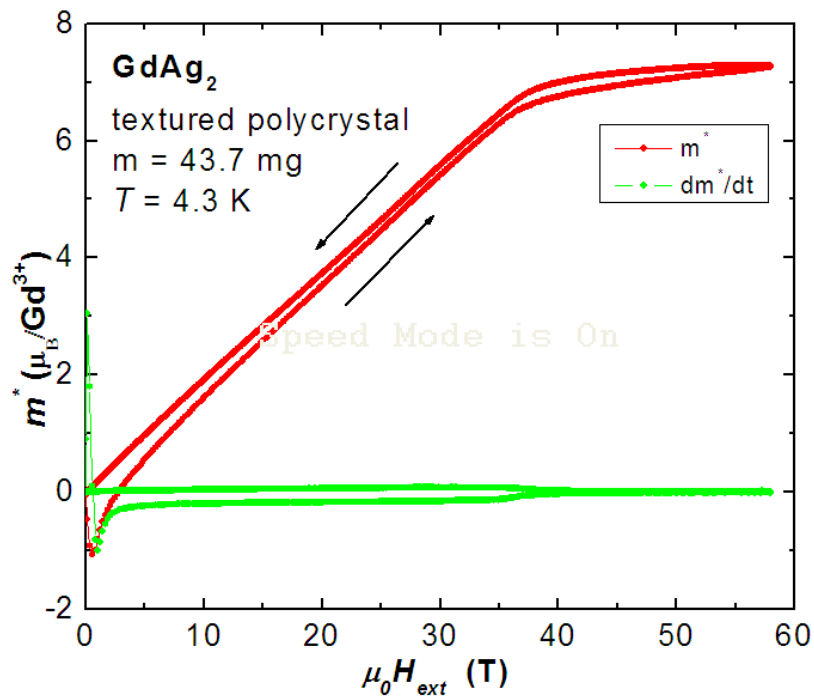


Figure 3.6 Isothermal magnetization at T = 4.3 K (Pulsed field at HLD).

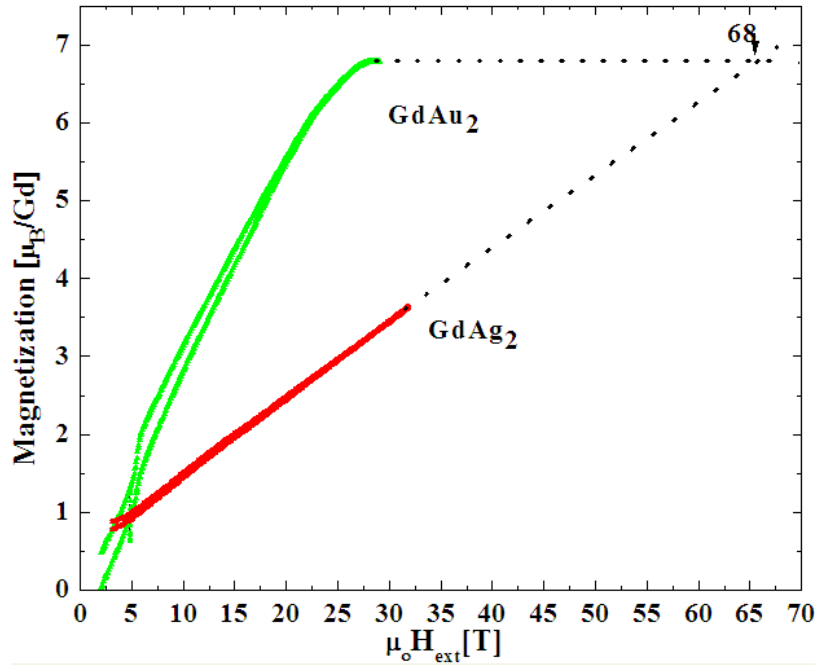


Figure 3.7 The dotted line is the linear extrapolation of isotherm of GdAg_2 , which meets the saturation moment of GdAu_2 at 68 T.

The saturation magnetic field can be calculated with the standard model. The Hamiltonian for the system can be derived as follows.

Since for a Gd^{3+} the 4f shell is half filled so $L=0$ filled and charge density is spherical, hence in first order perturbation theory there is no crystal field effect. Therefore the magnetic Hamiltonian for 4f, Gd^{3+} system is a sum of isotropic exchange (RKKY), the classical dipolar and the Zeeman interaction:

$$H = -\frac{1}{2} \sum_{ij} J_i^\alpha(j, \epsilon) \mathbf{J}_i \mathbf{J}_j - \frac{1}{2} \sum_{ij\alpha\beta} \mathbf{J}_i^\alpha J_{\text{CD}}^{\alpha\beta}(ij) J_j^\beta - \sum_i g_J \mu_B \mathbf{J}_i \mathbf{H} \quad (3.1)$$

In expression (3.1) the 4f moment of the i^{th} Gd^{3+} ion is represented by the three components of the angular momentum operator \mathbf{J}_i^α ($\alpha = 1, 2, 3$). g_J is the Lande factor and μ_B the Bohr magneton.

The classical dipolar interaction constant can be calculated as;

$$J_{\text{CD}}^{\alpha\beta}(ij) = (g_J \mu_B)^2 \frac{(\mathbf{R}_i^\alpha - \mathbf{R}_j^\alpha)(\mathbf{R}_i^\beta - \mathbf{R}_j^\beta) - \delta_{\alpha\beta} |\mathbf{R}_i - \mathbf{R}_j|^2}{|\mathbf{R}_i - \mathbf{R}_j|^5} \quad (3.2)$$

Here \mathbf{R}_i denotes the position vector of the i^{th} Gd ion, which is known from the crystallographic structure.

In order to calculate the saturation field we use the following equation for the Néel temperature T_N , the paramagnetic Curie temperature Θ_p and the saturation field H_s for the transition from the antiferromagnetic to the field-induced-ferromagnetic state,

$$\Theta_p = \frac{J(J+1)}{3k_B} \mathfrak{J}(0). \quad (3.3)$$

$$T_N = \frac{J(J+1)}{3k_B} \mathfrak{J}(\mathbf{Q}) \quad (3.4)$$

The ferromagnetic structure is reached at a field

$$H_s = \frac{J}{g\mu_B} [\mathfrak{J}(\mathbf{Q}) - \mathfrak{J}(0)] \quad (3.5)$$

Where H_s is a saturation field (critical field)

Combining equations (3.3), (3.4), and (3.5) we have saturation field H_s in term of Néel temperature (T_N) and paramagnetic Curie temperature (Θ_p)

$$H_s = 3k_B \frac{[T_N - \Theta_p]}{g_j \mu_B (J+1)} \quad (3.6)$$

Here τ is the propagation vector of the magnetic structure and k_B is Boltzman's constant. μ_B is Bohr magneton and g_j is the Lande factor. $\mathfrak{J}(\mathbf{Q})$ is the Fourier transform of the exchange, which is defined as

$$\mathfrak{J}(\mathbf{Q}) = \sum_j e^{-i\mathbf{Q}\cdot(\mathbf{R}_i - \mathbf{R}_j)} \mathfrak{J}(i,j) \quad (3.7)$$

By using equation (3.6) the saturation field can be estimated.

The paramagnetic Curie temperature Θ_p for GdAg₂ is -52 K [1991 Gig] and Neel Temperature is 22.7 K.

Since for Gd³⁺ the 4f shell is half filled it has spherical charge density and no orbital moment, therefore $L=0$, so $J = S = 7/2$

$$g_J = 1 - \left(\frac{J(J+1) + S(S+1) - L(L-1)}{2J(J+1)} \right) = 2 \quad (3.8)$$

By using the values of, Θ_p , T_N , J and g_J in equation (3.44) would give the value of saturation field $H_s = 37$ T. This calculated value agrees very well to experimental value found by M. Doerr and Yurii Scourski in pulsed magnetic fields as described in section 3.1.3.

3.1.4 Thermal Expansion of $GdAg_2$

The zero field thermal expansion measurement in the 4.2 K — 290 K range of temperature is shown in Fig 3.8. For the measurements, the sample was placed between the parallel plates of the dilatometer with sapphire. Since the sample was cubic, it was easy to place on a spacer. Then the two halves of the dilatometer were screwed together. It was then mounted on the dilatometer holder along with the sample stick and checked for electrical isolation. Note down the capacitance (for present work $C_0 = 3.9489$ pF). The dilatometer along with sample stick was slowly and carefully inserted into the Cryostat containing Helium liquid and a superconducting magnet.

The thermal expansion curve in Fig 3.8 (measured by dilatometry) was done at a polycrystal sample is shown with a solid curve. There is a negative thermal expansion coefficient (contraction) between 4.2 K and 23 K; above this temperature, a positive thermal expansion coefficient is observed.

The most important feature of present thermal expansion measurement is that when the relative change of length $\Delta l/l$ is compared with thermal expansions $\Delta c/c$, $\Delta a/a$ and $\Delta V/3V$, which were measured by X-ray powder diffraction [2007Rot], It is observed that $\Delta l/l$ matches well with thermal expansion along a-axis ($\Delta a/a$) as shown in Figure 3.8. It implies that the expansion was measured probably along a-axis, if it is so it means that the material is crystallographically textured. This becomes important when testing material with low crystalline-symmetry and anisotropic thermal expansion characteristics. The assumption that the measured length change corresponds to about a third of the volume change ($\Delta V/V = 3 \Delta l/l$) is no longer valid. So, it becomes necessary to specify the crystallographic directions along which measurements are made.

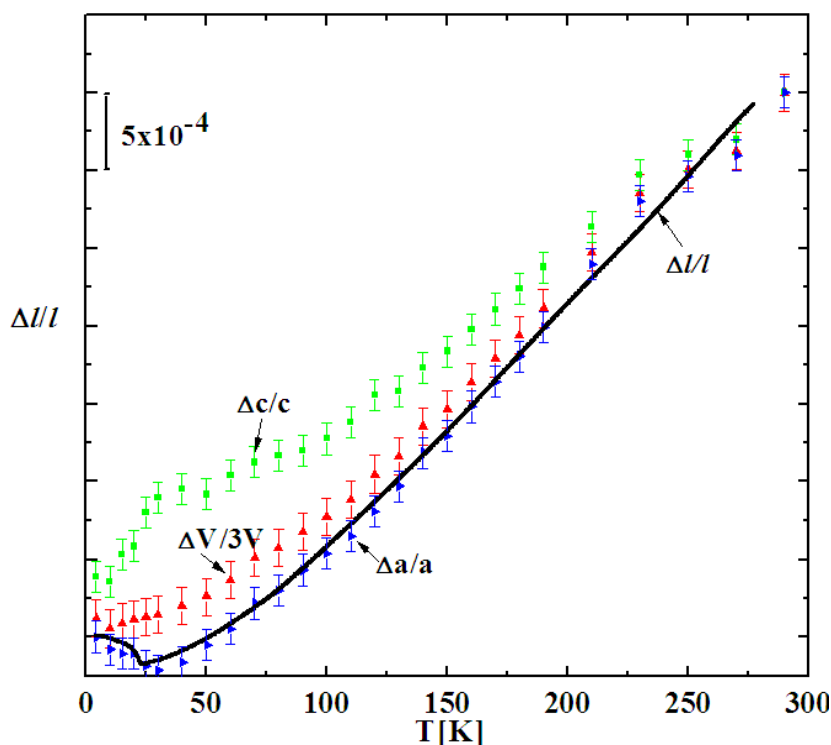


Figure 3.8 Comparison between the thermal expansion of GdAg_2 as measured by the dilatometer (solid curve) and by powder x-ray diffraction (from literature, points) [2007 Rot].

Verification of the texture in GdAg_2 sample was performed with GADDS (General Area Detector Diffraction System) instrument in Institute of Physical Chemistry (University of Vienna).

The sample was exposed to $\text{Cu K}_{\alpha 1,2}$ radiation. Sample to detector distance was about 15cm. ω is the incident angle of X-rays and 2θ is the angle of diffraction.

The measurements were made with continuous rotation of the specimen to various angles, φ with respect to plane containing the incident and diffracted beams over the entire 360° range. The exposure time for each frame with frame window 2° was about 60 min.

A bright spot as shown in figures 3.8a and 3.8b was observed at (213) and (204) orientation of the specimen at $2\theta = 59^\circ$ on Debye Scherrer rings indicates the preferential orientation. Figure 3.9a shows a strong texture. Reflection from planes (213) and (204) are also present in X-ray diffraction pattern (Figure 3.4).

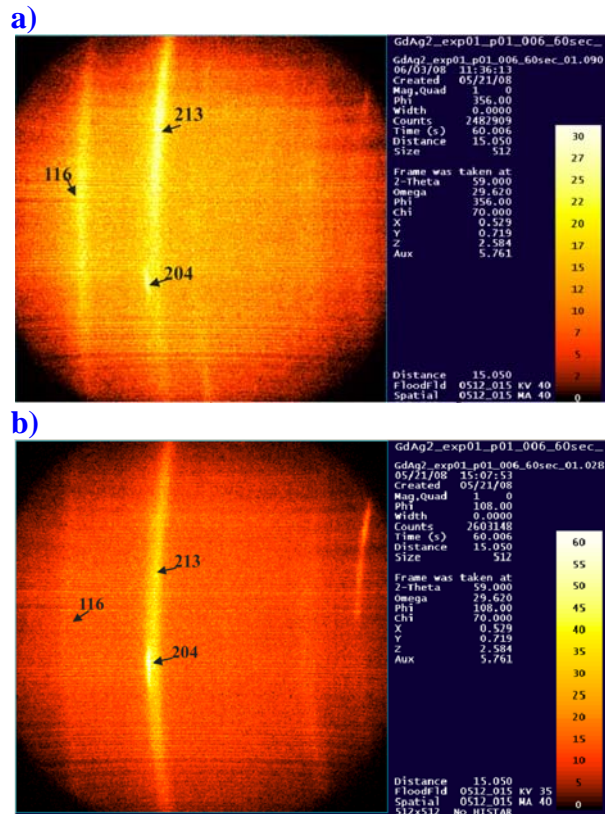


Figure 3.9 a) & b) The varying intensities along the arcs indicate a preferred orientation.

Moreover from thermal expansion between 4 K and 36 K two transitions at Temperatures ~ 11 K and 22.7 K are observed as shown in Figure 3.10. We can see these transitions more clearly in Figure 3.11, which is derivative of the Δ/l curve with respect to temperature vs. T [K](thermal coefficient α). The transition at $T_t = 10.8$ K as proved by neutron diffraction results, corresponds to a change in magnetic structure and the 2nd transition at 22.7 K corresponds to the Néel Temperature T_N , which identical with the value reported by [1991Gig]. The transition at 21.3 K, which was observed in neutron diffraction and specific heat measurements, is not observed in present measurement, reason may be that the transitions at 21.3 K and 22.7 K are very close and our measurement resolution is not high enough and the footprint of this transition in the magnetoelastic strain is small.

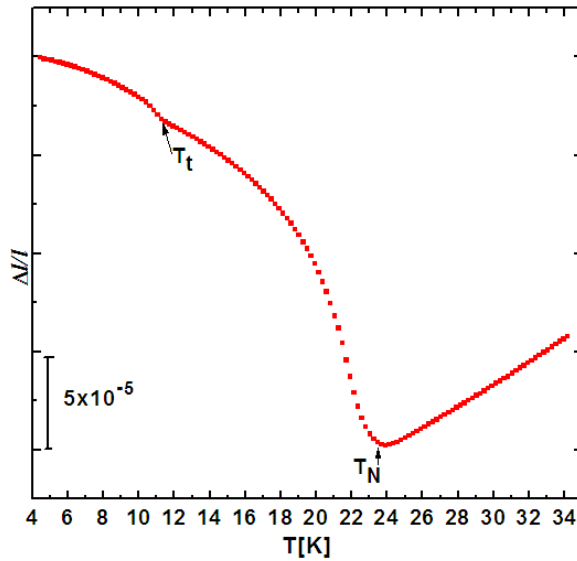


Figure 3.10 The thermal expansion of GdAg_2 at zero field. The arrows indicate the different transition temperatures.

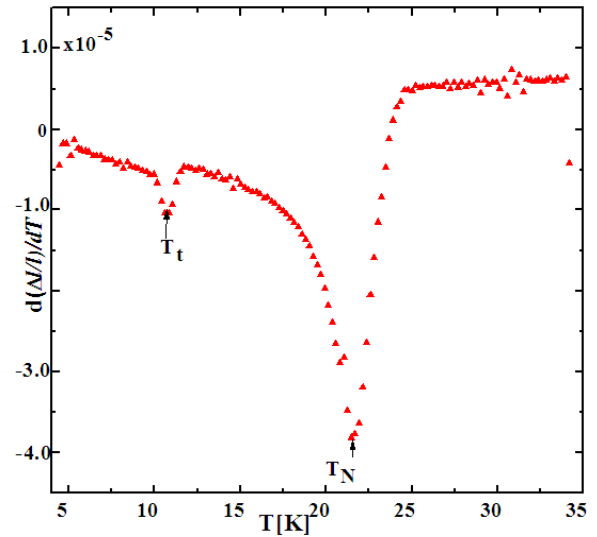


Figure 3.11 Derivative of thermal expansion with respect to Temperature Vs Temperature showing transition at T_t & T_N .

3.1.5 Magnetostriction

The magnetostriction measurements were performed along the parallel ($\lambda_{||}$) and perpendicular (λ_{\perp}) directions to the applied magnetic field (H_{ext}) at selected temperatures.

Figure 3.12 shows the longitudinal magnetostriction at seven different temperatures (4 K, 8 K, 10 K, 15 K, 22 K, 26 K, and 33 K) along the magnetic fields up to 9 T. Because of preferred orientation of crystal grains (texture), the magnetostriction may be considered as measured along a-axis $\lambda_{||} \sim (\Delta a/a)$. The arrows in the figure show whether the field was ramped up, or down so by following the direction of the arrows one also follows the cycle of the magnetic field. This cycle starts at magnetic field of 0 T goes up to 9 T and back to 0 T. The magnetostriction is positive from 4 K to 10 K. A steep increase in magnitude of $\lambda_{||}$ at 4 K and 8 K occurred in magnetic field around 1T. Note that single q phase transitions are often associated with symmetry breaking. But no such symmetry breaking is found in GdAg_2 (see fig 3.14) this is evidence of the “*magnetoelastic paradox*” The experimental data indicates, that similar to $\text{GdNi}_2\text{B}_2\text{C}$ the magnetoelastic paradox is only present in zero field and may be lifted by a small magnetic field. There might be a transition from a zero field multiple q structure to a single q structure in a magnetic field as it has been conjectured in

[2008Jenson & Rotter]. Above 1 T the magnitude of $\lambda_{||}$ increase but with very weak slope and exhibit a broad peak at $\mu_0 H = 5.5$ T. Above 5.5 T, the magnitude of $\lambda_{||}$ decrease steadily with the magnetic field and saturation is not achieved up to 9 T. The magnetostrictive effect is negligibly small above 10 K in a low field but at higher field, negative magnetostriction is observed. However, none of isotherm reaches the saturation in an applied field of 9 T. At 22 K above 3 T the magnetostrictive effect is higher than at other temperatures. We suggest that this behaviour can be explained: for temperature approaching $T \leq T_N$, the field induced spin reorientation transition to ferromagnetism occurs at very small fields and can be triggered by the experimentally available field of 9 T thus leading to a large negative magnetostrictive effect. At temperatures of 4 K and 8 K a small hysteresis in the data is also noticed, further more, the curves do not end at the point where they started reason might be that the sample has turned during the measurement (at higher temperatures this type of irreversibility is not seen and might therefore be single artefact for this measurement. The data recorded during the ramping down of the field are almost the same values recorded during ramp up of the field. No hysteresis is visible at temperatures higher than 10 K.

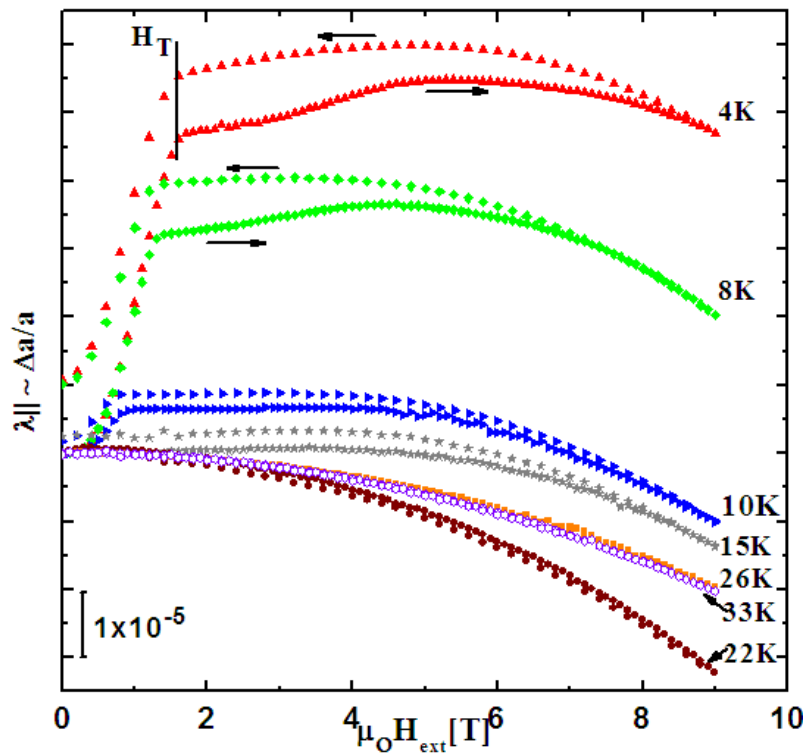


Figure 3.12 Longitudinal forced magnetostriction of textured GdAg₂ sample at different temperatures.

Figure 3.13 presents the perpendicular magnetostriction (λ_{\perp}) at different temperatures (4 K, 8 K, 10 K, 15 K, 22 K, and 33 K). Because of the texture, the magnetostriction may be considered as measured along a-axis $\lambda_{\perp} \sim (\Delta a/a)$ (textured sample) while the field applied perpendicular to it (not along a specific crystallographic direction, the field direction being different for each single crystal grain in the textured polycrystal). The isotherms from 4 K to 15 K are initially negative and then increase with positive slope up to field of 5 T, after which the slope becomes again negative. Near the Néel temperature, the magnetostriction increases linearly with negative slope and reaching the value of about $\lambda = -6 \times 10^{-5}$ at 9 T, which is $\lambda_{\perp} = 2\lambda_{\parallel}$ at 22 K.

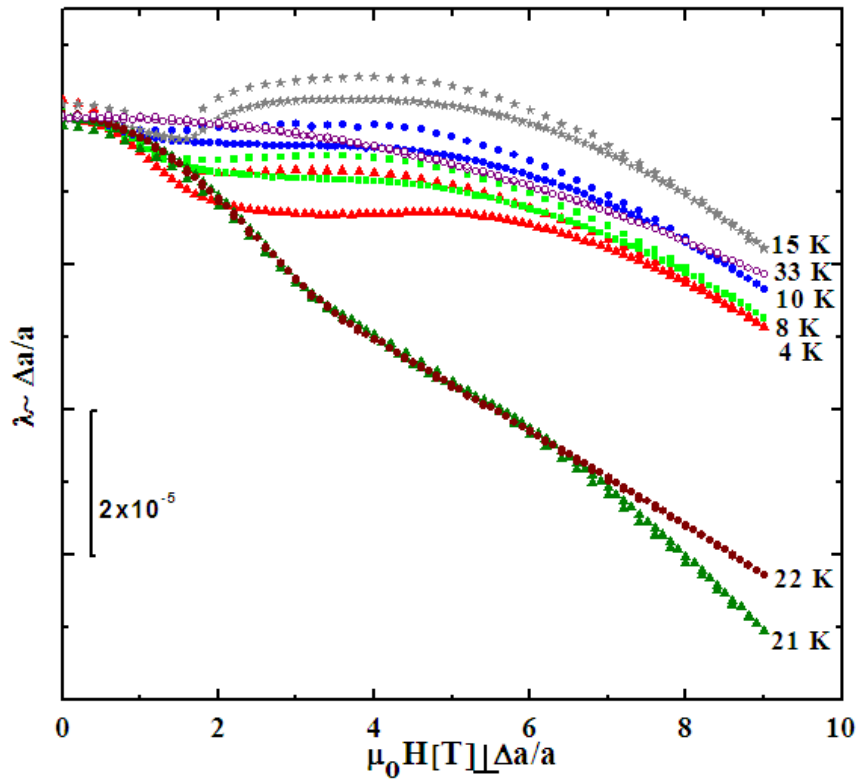


Figure 3.13 Perpendicular forced magnetostriction of textured GdAg_2 sample at different temperatures.

Figure 3.14 shows the comparison of magnetostriction parallel (λ_{\parallel}) and, perpendicular (λ_{\perp}) to the magnetic field measured at 4 K. Both magnetostrictions are of opposite in sign and show anisotropic behaviour at low field. Magnetostriction (λ_{\parallel}) measured parallel to the magnetic field approximately 2.5 times greater than magnetostriction (λ_{\perp}) measured perpendicular to the magnetic field at 4 K. In perpendicular

magnetostriction the direction of applied field is not known so it is believed that the direction of field was along $\frac{1}{2}(b+c)$ orientation, which mean it is mix behaviour of aHb and aHc! Therefore, aHb could be larger signal. The magnetic anisotropy is decreasing with increasing temperature and at 33 K it completely vanishes as shown in figure 3.14.

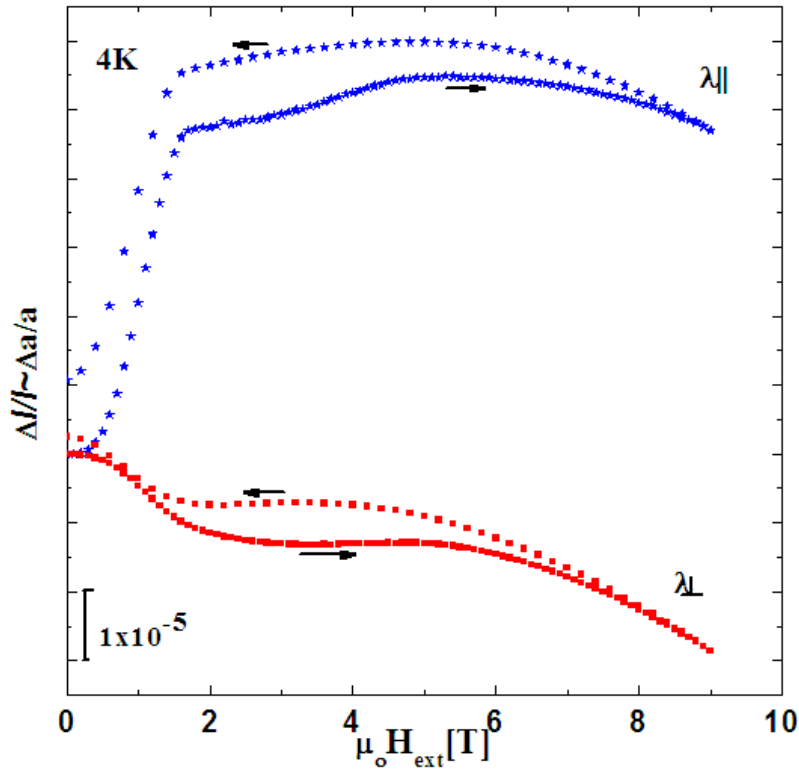


Figure 3.14 Comparison of the longitudinal (open symbols) and perpendicular (closed symbols) magnetostriction curves of the textured GdAg₂ at temperature 4 K and 33 K.

Figure 3.15 shows the comparison of the temperature dependence of thermal expansion $\Delta l/l$ under an applied magnetic field of 0 T, 1.5 T and 9 T. It can be seen that almost all the curves have the same behaviour and by increasing applied magnetic field the negative thermal expansion increases. At temperature near $T_N = 22.7$ K the thermal expansion changes from negative to positive.

If we shift the zero field thermal expansion curve to match the curve at 1.5 T (the shifted curve is shown by solid line) the value of thermal expansion at 4 K by increasing field from 0T to 1.5 T is about 4.8×10^{-5} . This value corresponds exactly to the value of magnetostriction measured at 4 K and at 1.5 T, (see Figure 3.12).

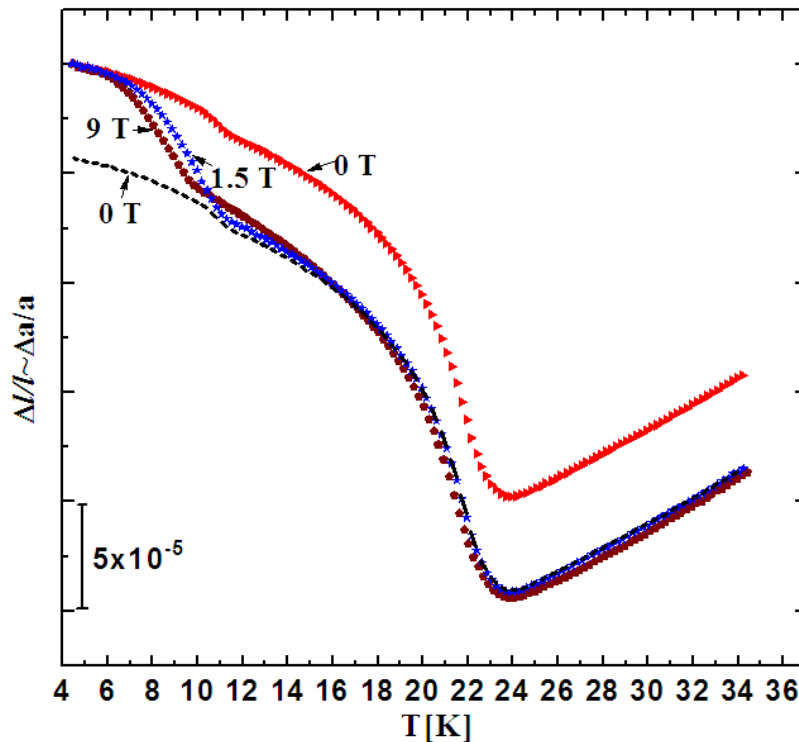


Figure 3.15 Thermal expansion of GdAg_2 parallel to applied field direction at $H = 0$ T, 1.5 T, and 9 T

3.2 $\text{PrFe}_4\text{As}_{12}$

Ternary skutterudites $\text{RE}_y\text{TM}_4\text{X}_{12}$ with RE=rare-earth, TM = Fe, Co, Rh, Ru... and X=P, As, Sb attracted much interest because of a variety of possible ground states and because of their large thermoelectric potential.

Skutterudites based on Pr exhibit a number of outstanding features. Among them are superconductivity in $\text{PrRu}_4\text{As}_{12}$ and $\text{PrRu}_4\text{Sb}_{12}$ below 2.4 and 1 K, respectively [1997Shi, 2000Tak], a metal to insulator transition in $\text{PrRu}_4\text{P}_{12}$ at $T_{\text{MI}} = 60\text{K}$ [1997Sek] antiferromagnetic ordering at T_{N} in $\text{PrFe}_4\text{P}_{12}$ [1987Tor]. Kondo-like anomalies in transport phenomena were found for the latter and C_p/T for $T \rightarrow 0$ shows a huge value of about 1.4J/molK^2 [2000Sat, 2000Mat]. While a great deal of research has been performed on the Pr-based filled, skutterudite phosphides and antimonides but there have been only a few investigations of the Pr-based filled skutterudite arsenides. The $\text{PrT}_4\text{As}_{12}$ ($T = \text{Fe, Ru, Os}$) compounds were all originally synthesized and their lattice parameters measured by Braun and Jeitschko, [1980Bru]. $\text{PrFe}_4\text{As}_{12}$ is

found to become ferromagnetically ordered below a Curie temperature $T_c = 18$ K, [2008Say].

3.2.1 Single crystal growth and structure

The Pr-based Single-crystal filled skutterudite arsenides $\text{PrT}_4\text{As}_{12}$ ($T = \text{Fe, Ru, Os}$) were grown from high purity elements by mineralization in a Cd : As flux [2008Hen]. The process was carried out over 3 - 4 weeks in sealed quartz ampoules with pressures of 15 - 40 atm. The elevated pressures were produced by As vapours and Ar gas at the mineralization temperatures between 750 – 825 °C. To avoid an explosion, the ampoules were heated in a custom-built pressure cell. Typical dimensions of grown single crystals were 0.5 – 2.5 mm.

The crystal structure has been determined at room temperature by using a four circle X-ray diffractometer with a 2D-CCD[2008Hen], The structure was resolved by the full matrix least squares method using SHELX-97

$\text{PrFe}_4\text{As}_{12}$ has cubic structure,(Figure 3.16) and the space group is Im-3 with lattice parameter, $a = 8.310(2)$ Å As site: $x = 0.1541, y = 0.3447, z = 0$ site occupation: Fe = 0.99, As = 0.99, Pr=1.00 Displacement parameters: Fe = 3, As = 4, Pr = 9 [$\text{Å}^2 \times 10^3$]

Discrepancy factors ($R1/wR2$): 3.72/8.12%

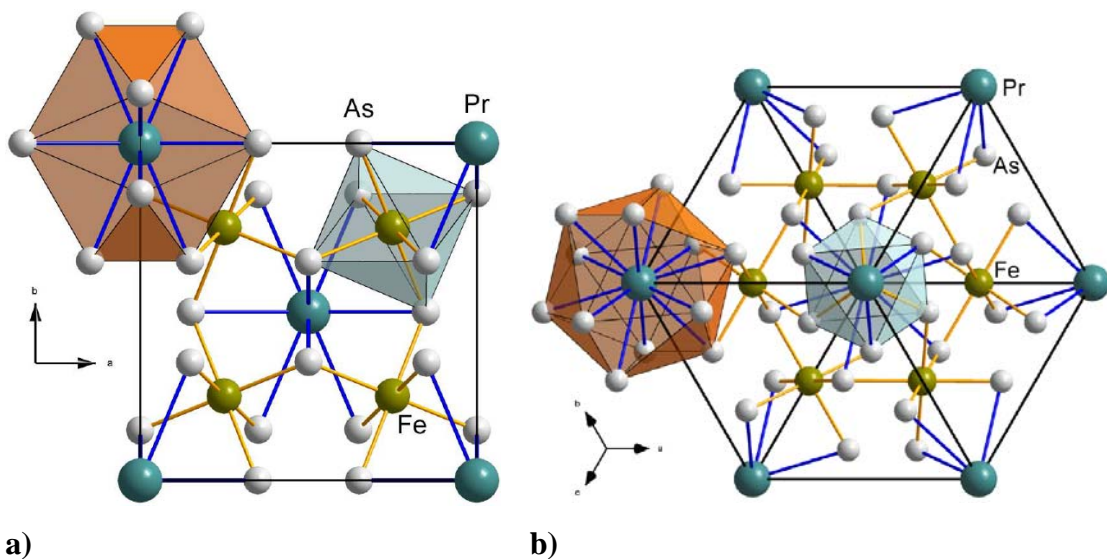


Figure 3.16 (a)Crystal structure of skutterudite $\text{PrFe}_4\text{As}_{12}$ (b) Three-dimensional view of unit cell in $\text{PrFe}_4\text{As}_{12}$ [2008Hen].

3.2.2 Thermal expansion of PrFe₄As₁₂

The zero field thermal expansion between 4.2 K and 50 K was performed at the Technical University Vienna with the miniature capacitance dilatometer. The crystal was tiny and it was not easy to mount the crystal on the cell holder. To prevent the crystal from falling or turning in the field it was glued to the head of a screw. Epoxy-glue was used. The screw with the crystal on the top of it was put into the dilatometer through the bore in the upper housing and screwed with a brass nut. Then the other half of the dilatometer was imposed and the two halves were screwed together. After this, the dilatometer was mounted on the holder in the desired set up.

The resulting length change of the material can be seen in Figure 3.17. Spontaneous magnetostriction is observed when cooling below 18 K with a value of $\Delta l/l = -8 \times 10^{-5}$. Thermal expansion indicates ferromagnetic ordering below 17.8 K (spontaneous moment developed) close to the value of T_C . From the thermal expansion coefficient a very slight kink is observed at $T = 12$ K associated with a peak at 11.9 K. shown in the Figure 3.18 and in the inset of this figure which is the temperature derivative of the relative length change.

Above T_c negative thermal expansion is observed up to the maximum measured temperature (50 K).

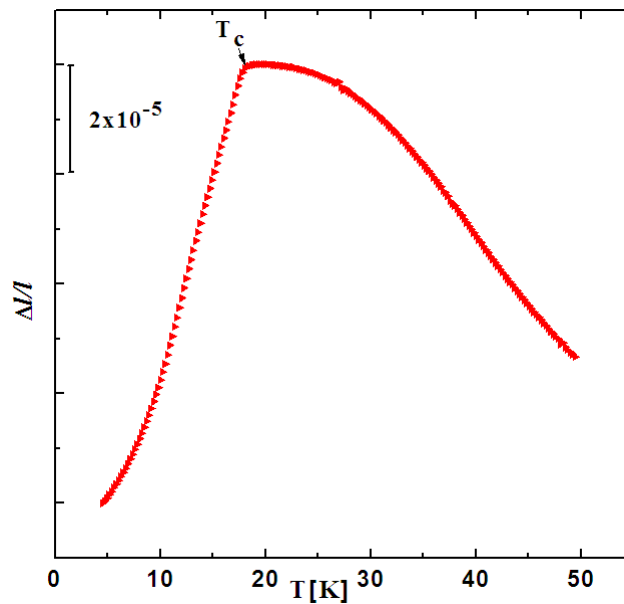


Figure 3.17 Thermal expansion of the PrFe₄As₁₂ single crystal along the a-axis from 4 to 50 K.

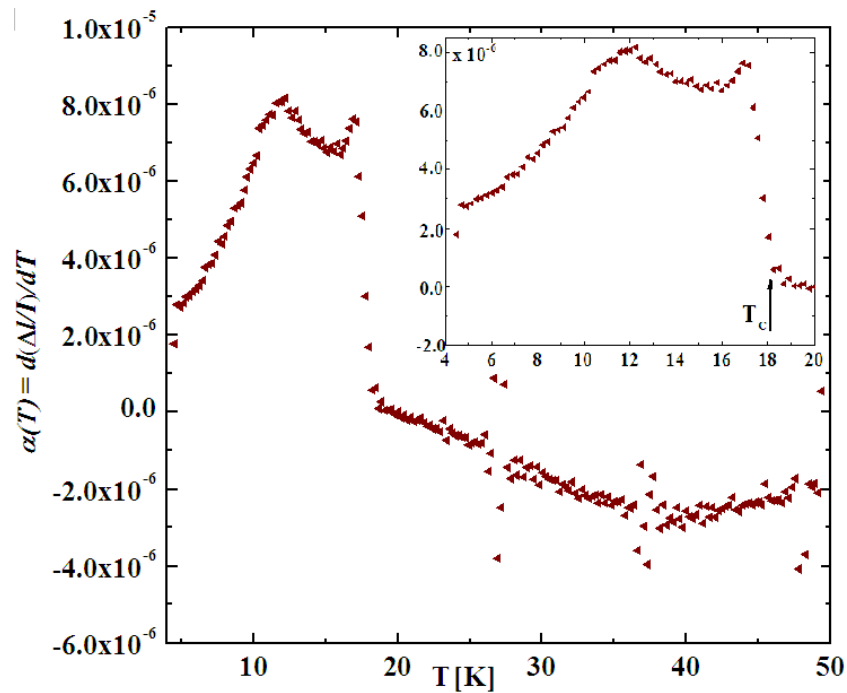


Figure 3.18 Derivative of relative length change with respect to temperature vs temperature.

3.2.3 Magnetization Study

From literature magnetization of PrFe₄As₁₂ has clearly shown that the compound orders ferromagnetically below 18 K. Magnetization M(H) isotherms' at T = 2 K along the [111] and [100] directions have revealed a saturated moment of 2.3 μ_B /f.u at 5.5 T. Figure 3.19 shows a change of easy axis from [100] to the [111] directions at H~ 0.6 T.[2008Say].

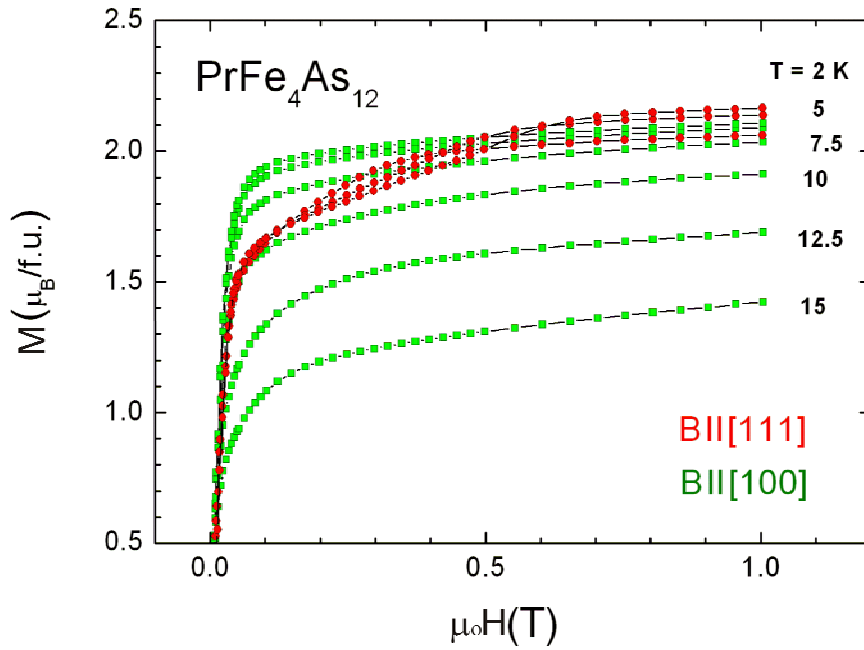


Figure 3.19 Magnetization, M , vs magnetic field, H , for different temperatures and field along the [111] (squares symbols) and [100] (circle symbols) crystallographic directions [2008Say].

3.2.4 Magnetostriction of $\text{PrFe}_4\text{As}_{12}$

The magnetostriction was measured for [100] and [111] directions along and perpendicular to the magnetic field.

Figure 3.20 shows the transversal magnetostriction at seven different temperatures (4K, 8K, 10K, 14K, 16K, 18K, and 20K) along [100] direction and magnetic fields up to 1 T along [010] direction. The arrows in the figure show whether the field was ramped up, or down. So by following the direction of the arrows one also follows the cycle of the magnetic field. This cycle starts at magnetic field of 0 T and goes up to 1 T and back to 0 T. It is observed that the magnetostriction is largest at 4 K and its value is about $\lambda_{100}(H_{||010}=1\text{ T}) = 1.4 \times 10^{-4}$. The magnetostrictive effect decreases with increasing temperature and at 18 K and 20 K the magnetostrictive effect is almost $< 1 \times 10^{-5}$. At 4 K Small hysteresis in the data appears which becomes smaller with increasing temperature and vanishes at 16 K and above.

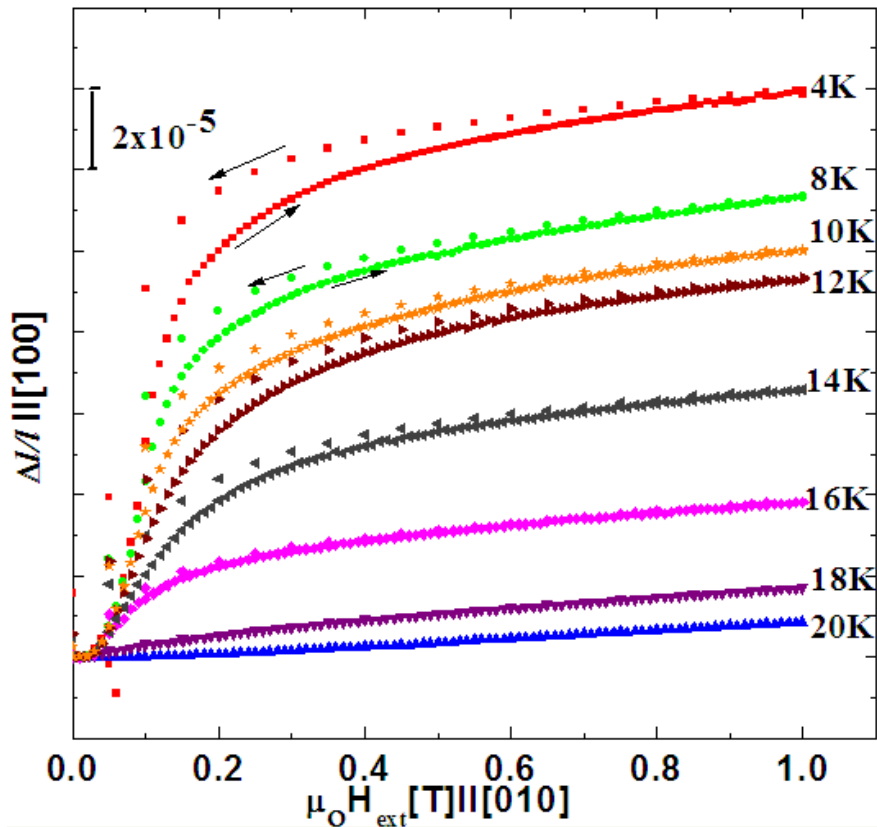


Figure 3.20 Transversal Magnetostriction of the $\text{PrFe}_4\text{As}_{12}$ single crystal along [100] with magnetic field applied along [010]-direction up to 1 T at different temperatures.

Figure 3.21 shows the longitudinal magnetostriction $\lambda_{||}$ along [100]-axis. As we see there is a very small expansion and it is about a factor of 4 smaller in magnitude than the transversal magnetostriction. Isotherms of longitudinal and transversal magnetostriction show nearly the same qualitative behavior. The difference between the two data sets is that in longitudinal magnetostriction there is no hysteresis and also there is the irregularity that the 4 K and 8 K curves cross each other at $\mu_0 H = 0.35$ T. It seems very interesting that the crossing of 4 K and 8 K curves appears for both directions as we will see in longitudinal magnetostriction along [111] (see figure 3.23) and it confirms a change in magnetic structure between these two temperatures.

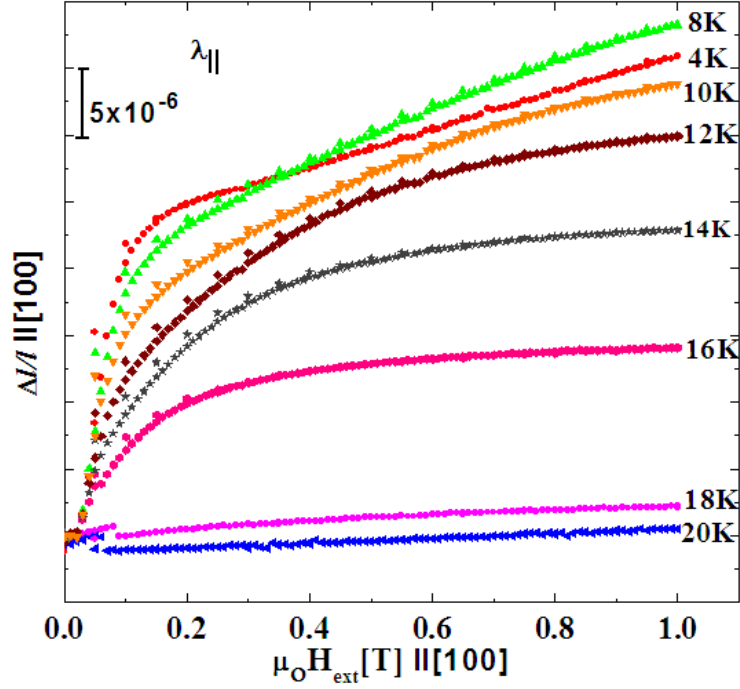
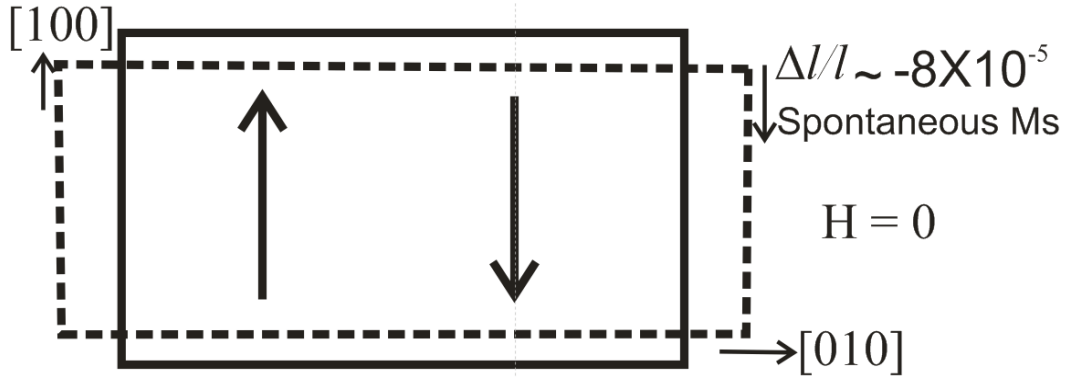


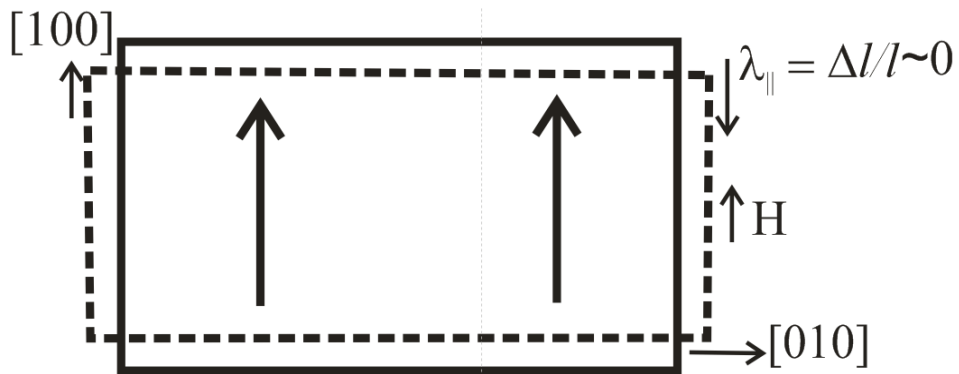
Figure 3.21 Longitudinal Magnetostriction of the $\text{PrFe}_4\text{As}_{12}$ single crystal along $[100]$ with magnetic field applied along same direction up to 1 T at different temperatures.

The data cannot be explained by a random domain distribution in zero field (because this would imply a zero volume change upon application of the magnetic field). A possible microscopic model to explain the zero field thermal expansion and forced magnetostriction along and perpendicular to magnetic field for the domain distribution is shown schematically in Figure 3.22. In zero field we assume two magnetic domains to be present these are represented by two arrows with opposite orientation, i.e., one along $[100]$ and other along $[-100]$ direction as shown in Figure 3.22a. As explained in section 3.2.2 it is assumed that below 18 K there is ferromagnetic ordering, and observed that below the 18 K temperature there is negative spontaneous magnetostriction with a value of $\Delta l/l_{100} = -8 \times 10^{-5}$. In Figure 3.22a the negative thermal expansion (spontaneous magnetostriction is represented by a dashed rectangle with which arrow indicates that the crystal shrinks by $\Delta l/l = -8 \times 10^{-5}$ along the $[100]$ -axis. From a forced magnetostriction along the $[100]$ -axis with respect to field along $[100]$ -axis (Figure 3.21) there is observed a negligibly small expansion $\lambda_{||} \sim 0$ as compared to the transversal magnetostriction along the $[100]$ -axis with respect to the field along the $[010]$ -axis (Figure 3.20). Such a small signal can be explained by our model: the magnetic field just turns the anti-parallel domain along the direction of field as shown in Figure 3.22b. As we can see from figure 3.20 there is a considerable amount of

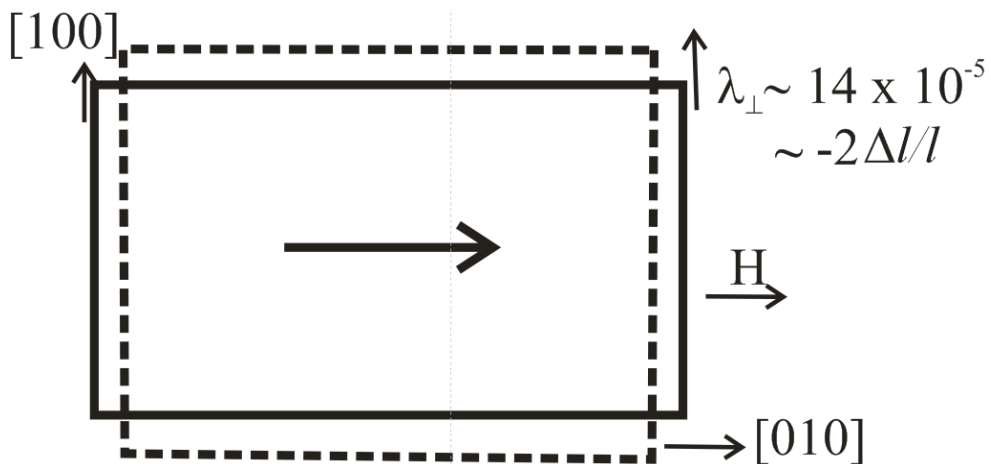
expansion and its value is about $\lambda_{\perp} = 1.4 \times 10^{-4} \sim -2 \Delta / l_{100}$ when we measure the transverse magnetostriction along the [100]-axis with respect to field along [010]-axis. This is explained in our model by the dashed rectangle as shown in Figure 3.22c.



(a) Dashed rectangle indicates that the crystal shrinks along the [100]-axis (measured direction) when cooling below T_C (Spontaneous Magnetostriction)



(b) The domain turned following the direction of field.



(c) Expansion along the [100]-axis with respect to field along 010-axis.

Figure 3.22 domain distribution models to explain the magnetostriction in $\text{PrFe}_4\text{As}_{12}\dots$ (For explanation see text).

3.2.5 Magnetostriction along the [111] direction

Figure 3.23 shows the graph of longitudinal magnetostriction along [111] direction with magnetic field along [111] direction at different temperatures. The magnetostriction is negative, increases with decreasing temperature and reaches the value 1×10^{-4} at 4 K. The magnetostriction at 4 K along [111] direction is 4.5 time greater the magnetostriction along [100] direction. By comparing the isotherm at 4 K of longitudinal magnetostriction along [111] and along [100] direction it shows a change in the easy axis from the [100] to the [111] directions at $H \sim 0.6$ T as observed in magnetization measurement (figure 3.18) [2008say], it looks relatively similar to that of iron and it seems that the easy direction is also [100], but probably there is moment on both Fe and Pr atoms.

Figure 3.24 shows the magnetostriction along [111] direction with magnetic field perpendicular to [111] direction. The direction of field is unknown. The magnetostriction is positive and maximum is at 4 K and its value is almost equal to the longitudinal magnetostriction along [100]. The magnetostrictive effect is decreasing with increasing temperature and at 20 K it becomes zero.

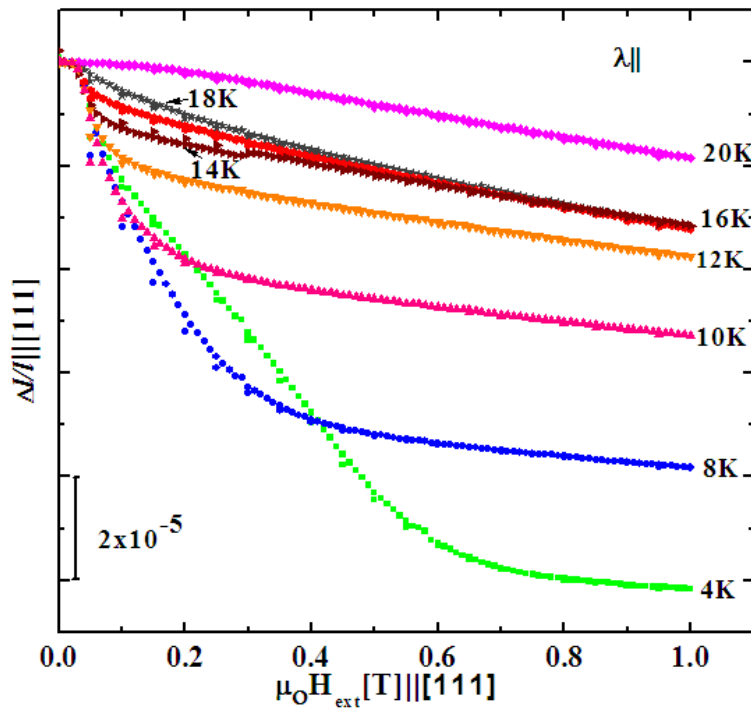


Figure 3.23 longitudinal measurements of the $\text{PrFe}_4\text{As}_{12}$ along [111] with magnetic field applied along [111] direction up to 1 T at different temperatures.

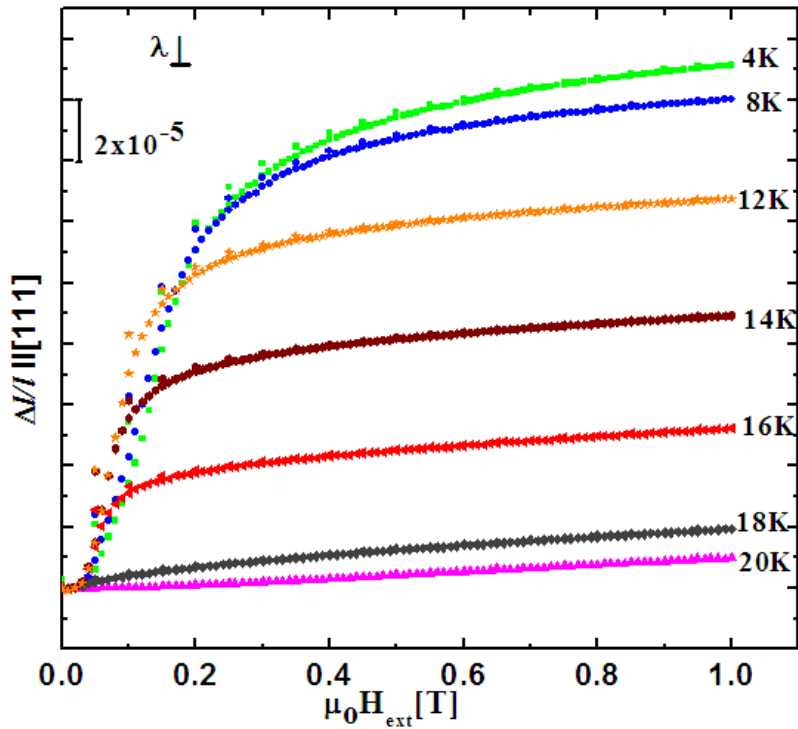


Figure 3.24 Transversal magnetostrictions of the $\text{PrFe}_4\text{As}_{12}$ along [111] with magnetic field applied perpendicular to [111] direction.

3.3 GdVO_3

The perovskites RVO_3 ($\text{R} = \text{Rare-earth}$) have attracted much attention in the past few years due to their intriguing magnetic properties, which result from the quasi, one-dimensional orbital character and a strong interplay between orbital and spin degrees of freedom [2007Tun, 2003Ulr, 2003Mot, 2004Miy, 2005 Miy].

The GdVO_3 compounds have been reported with numerous anomalous magnetic properties including low field history sensitive magnetic properties (L. D Tung in his paper [2005Tun] reported that the ZFC curves show a diamagnetic response at low temperatures and he investigated that this is due to the presence of small (negative) field during cooling: this negative field either comes from the trapped field of the superconducting magnet of SQUID magnetometer or the earth magnetic field at that location), multiple field-induced phase transitions at 1.8 K, and magnetization reversal related to a magnetic memory effect along the a-axes at about 8 K [2006Tun]. These had not been detected previously by earlier studies of polycrystalline [1995Kim, 1977Sak, 1956Boz] and single crystal samples [2003Miy].

Figures 3.25 and 3.26 show the magnetization characteristics of the GdVO₃ single crystal obtained in 0.1 kOe field using the field-cooled cooling (FCC) field-cooled warming (FCW) protocols and the magnetic isotherms at different temperatures along the main axes respectively [2006Tun]. Both data are discussed in detail elsewhere [2006Tun], the main features are included here. The magnetic reversal was observed along the *a*-axis at two different temperatures denoted as T_o and T_s . The values of T_o and T_s are dependent on the applied field but at a field $H = 0.5$ kOe there is neither magnetization reversal nor any anomaly around T_s and T_o was observed [2006Tun]. An antiferromagnetic (AF) spin ordering (SO) transition at $T_{so} = 118$ K and a transition at the temperature T_M of about 8 K was observed in magnetization as well as in heat capacity data [2006Tun].

From magnetic isotherms field induced transitions (Figure 3.26) were observed along the *a* and *b* axes. Hysteresis is visible along all the main axes below 8 K, however disappears above this temperature. The magnetization is saturated with a slight anisotropy in the magnetization values obtained along different axes at applied field 50 kOe and temperature 1.8 K as shown in Figure 3.26(a) and its value is about $6.7 \mu_B$ /f.u. Since this value is very close to a theoretical value of $7\mu_B$ for a Gd^{3+} free ion and much larger than $2\mu_B$ for V^{3+} free ion we conclude that the main contribution to the saturation magnetization arises from the Gd moments.

L. D. Tung et al. performed magnetic X-ray scattering experiments on a single crystal of GdVO₃ aligned along [100] directions, [private communication with L. D. Tung]. The following results were observed: at temperatures below 10 K, the Gd moments order in 4 different competing magnetic phases and a forced field ferromagnetic state at applied field above 3 T. At 2.4 K and zero field, (Figure 3.27) the Gd moments order with the propagation vector (0, 0.833, 0) (AF1 phase) which does not change significantly up to 0.75 T. At 1 T, the propagation vector shifts to (0, 0.84, 0) (AF2 phase). This corresponds well to a jump observed at around 0.9 T in both the magnetisation and magnetostriction data. At around 1.75 T, the third magnetic phase (AF3) appears with two distinct peaks located at around (0, 2.793, 2) and (0, 2.892, 2). These two peaks were slightly moved to higher *k* values when increasing the applied field. At 2.75T, the compound changes to a new magnetic phase with propagation vector of about (0, 0.759, 0) (AF4) before reaching the forced ferromagnetic state (F) at 3.25 T.

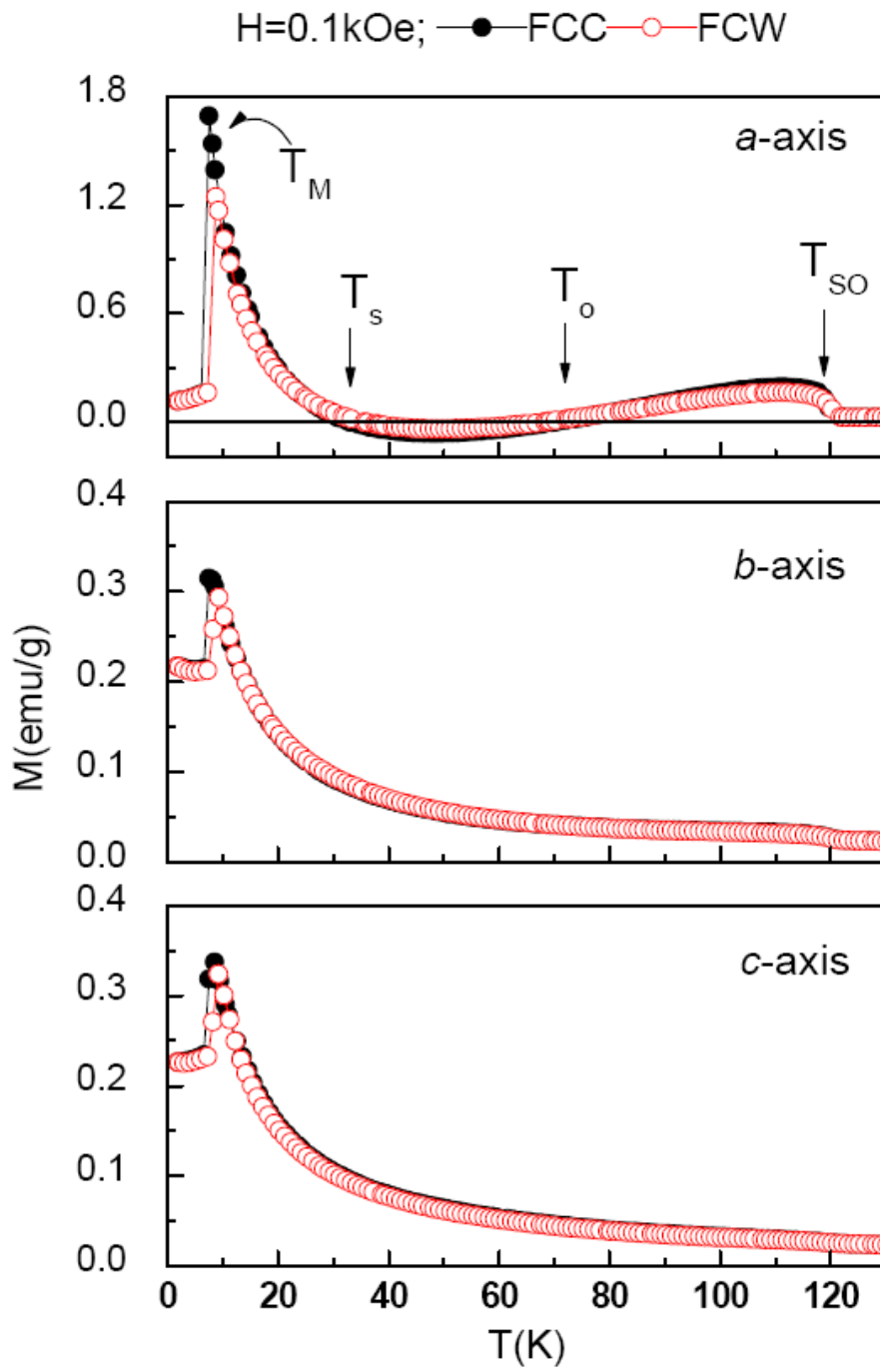


Figure 3.25 (colors line): FCC, FCW magnetization of the GdVO₃ single crystal measured at 0.1 kOe along the main axes [2006Tun].

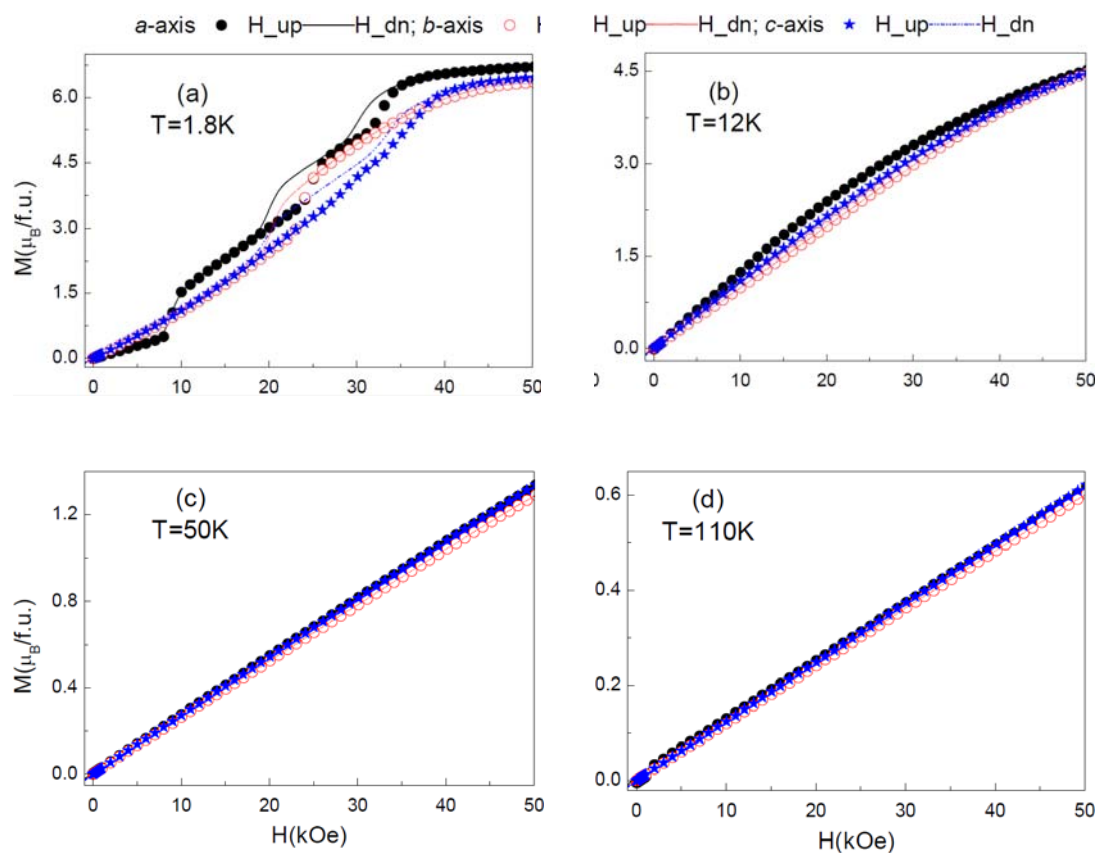


Figure 3.26 (colors online): The magnetic isotherms of the GdVO_3 single crystal measured along the main axes at different temperatures: 1.8 K (a); 12 K (b); 50 K (c) and 110 K (d). The symbols correspond with increasing field sections, lines with decreasing sections [2006Tun].

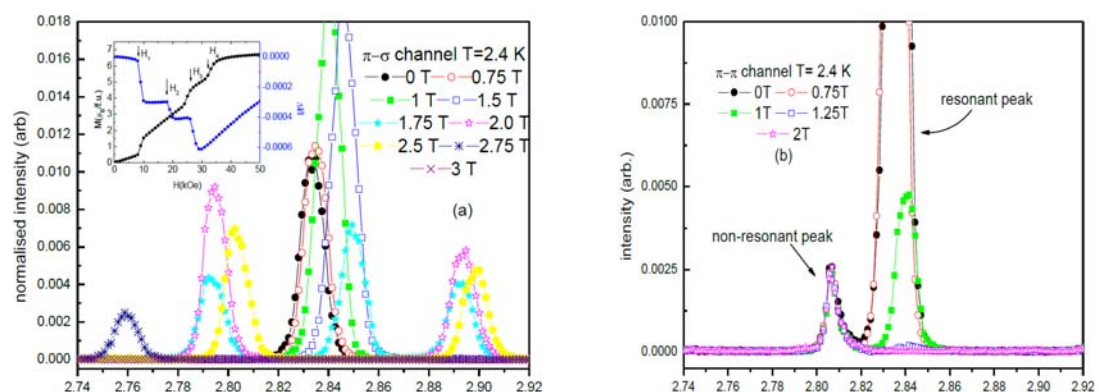


Figure 3.27 (colors) : Magnetic X-ray scattering signals obtained from the π - σ channel (a) and π - π channel (b) with the k-scan at 2.4 K. The inset in (a) shows the results of the magnetisation and the magnetostriction curves measured at 1.8 K [L. D. Tung].

The positions of the three transitions AF2-AF3, AF3-AF4, and AF4-F observed in the X-ray scattering data were found in good agreement with the magnetisation and magnetostriction data.

A magnetic phase diagram for k-scan with temperature at different magnetic fields of 0, 1.0, 2.0, and 3.0 T was constructed [private communication from L. D. Tung] is presented in Figure 3.28. The phase diagram of the GdVO₃ compound has been derived from the magnetic X-ray scattering. It is discovered that, when warming the sample in zero or small magnetic field, the Gd moments first transform from AF1 to AF4 phase at $T_1=7$ K before becoming paramagnetic (P) at $T_2 = 8$ K. The small temperature window of 1.0 K between T_1 and T_2 , in which the AF4 phase exists, was not detected previously (2006Tun). The magnetic memory effect as well as the magnetisation reversal seems to occur also at T_1 [private communication with L. D. Tung].

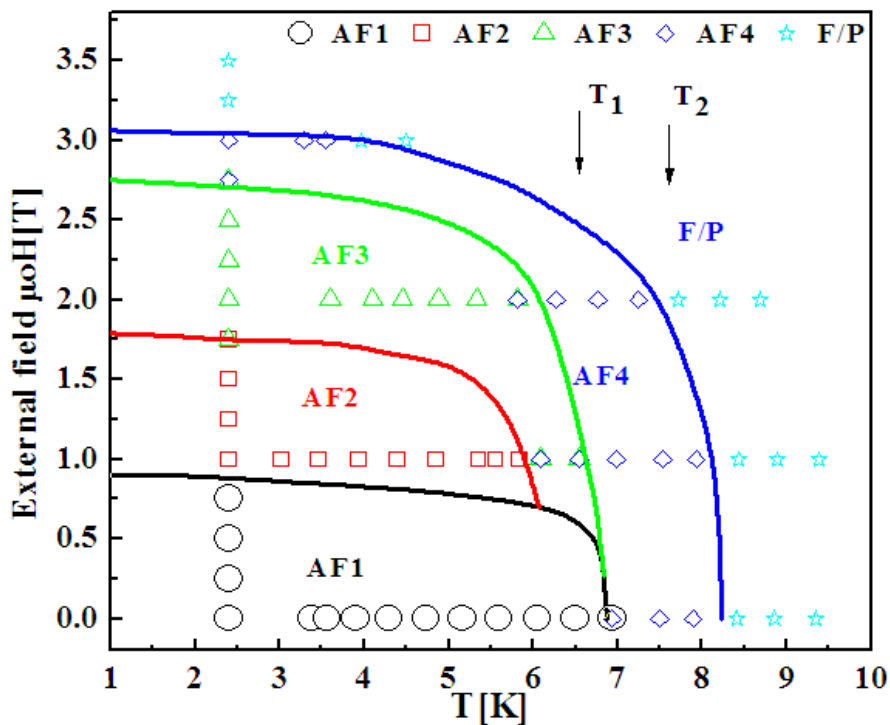


Figure 3.28 (colors) Magnetic phase diagram for the Gd magnetism in a GdVO₃ single crystal as derived from magnetic X-ray scattering. The magnetic field was applied along the a-axis, the symbols are experimental data, and the lines separating the phases are guide to the eyes. The measurements were carried out with increasing temperature [Private communication with L. D Tung].

In the present work, thermal expansion and magnetostriction measurements were made on single crystal of GdVO_3 grown by means of the floating zone technique using a high temperature xenon arc furnace. The sample size was about $1.39\text{mm} \times 1.92\text{mm} \times 2.29\text{mm}$. Measurements were carried out using a sensitive capacitance dilatometer. The thermal expansion was measured from 2.4 K to 10 K in the 0 magnetic field and field up to 4 T along [100] direction. The longitudinal magnetostriction was measured on a single crystal at selected temperatures with magnetic field up to 7 T along the [100] and [011] directions. The purpose of our measurements was to investigate how the transitions between several magnetic phases show up in magnetostriction measurements and to verify the phase diagram of the GdVO_3 compound derived from the magnetic X-ray scattering shown in Figure 3.28.

3.3.1 Thermal expansion along [100] direction

The linear thermal expansion of GdVO_3 single crystal measured along [100] crystallographic direction at different magnetic fields of $\mu_0 H = 0$ T, 0.5 T, 1 T, 1.5 T, 2 T, 2.5 T, and 4 T in temperature range 2.4 K to 10 K is shown Figure 3.29. Several anomalies were observed below 9 K and applied field $\mu_0 H \leq 3$ T and these anomalies shifted towards low temperature with increasing magnetic field. These anomalies indicate transitions between different magnetically ordered states.

Zero field and 0.5 T curves show small linear thermal expansion up to 7.5 K. Jumps were observed at temperatures around ~ 7.6 K and ~ 9 K. According to the phase diagram (Figure 3.32) a jump at 7.6 K corresponds to the phase transformation AF1 to AF4 phase this phase transformation was observed at $T_1 \approx 7$ K in magnetic X-ray scattering. The transition at ~ 9 K indicates that the Gd moments enter a paramagnetic phase. At external field $\mu_0 H = 1$ T, 1.5 T and 2 T three transitions were observed, corresponding to AF2 \rightarrow AF3 \rightarrow AF4 \rightarrow paramagnet. At 4 T the thermal expansion was almost linear. Moreover, the magnitude of the expansion of the crystal increases with increasing field.

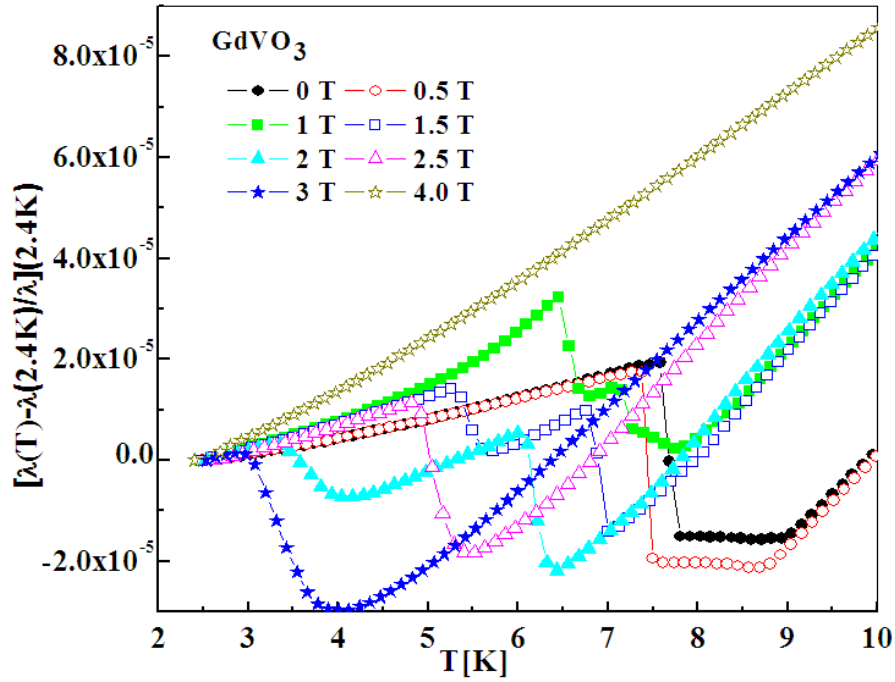


Figure 3.29 The thermal expansion of a GdVO₃ single crystal measured along [100] direction at $\mu_0H = 0, 0.5, 1, 1.5, 2, 2.5, 3, 4$ T.

3.3.2 Magnetostriction of GdVO₃

The magnetostriction of GdVO₃ single crystal was measured long [100] and [011] directions with magnetic field up to 7 T directed parallel ($\lambda_{||}$) to the crystallographic directions.

Figure 3.30 and 3.31 show the results of the longitudinal magnetostriction at selected temperatures from 2.4 K, to 5 K and 6.5 K, to 20 K respectively. Note that the same scale was used for both data and the magnetostriction curves are shifted along the vertical axis for the sake of clarity. Several anomalies accompanying the magnetic phase transition were observed. Four magnetic phase transitions were observed in temperature range 2.4 K—7 K, three of them are staircase like up to 3 T and one is observed above 3 T. The number of magnetic phase transitions is decreasing with the increase of temperature. At temperatures $7 \text{ K} < T \leq 15 \text{ K}$ only one transition was observed at $H \sim 5 \text{ T}$ which shifted little bit to lower field at 15 K temperature. No magnetic transition was observed above 15 K temperature and magnetic field above 6 T. The magnetostrictive effect was negligible small above 15 K. A small hysteresis in the data appeared in the temperature range 2.4 K to 15 K and magnetic field between 4

T and 5 T. Furthermore, the measured curves show that the field values for the transitions are the same for increasing and decreasing field ramps except the transition at 5 T where the hysteresis also appeared.

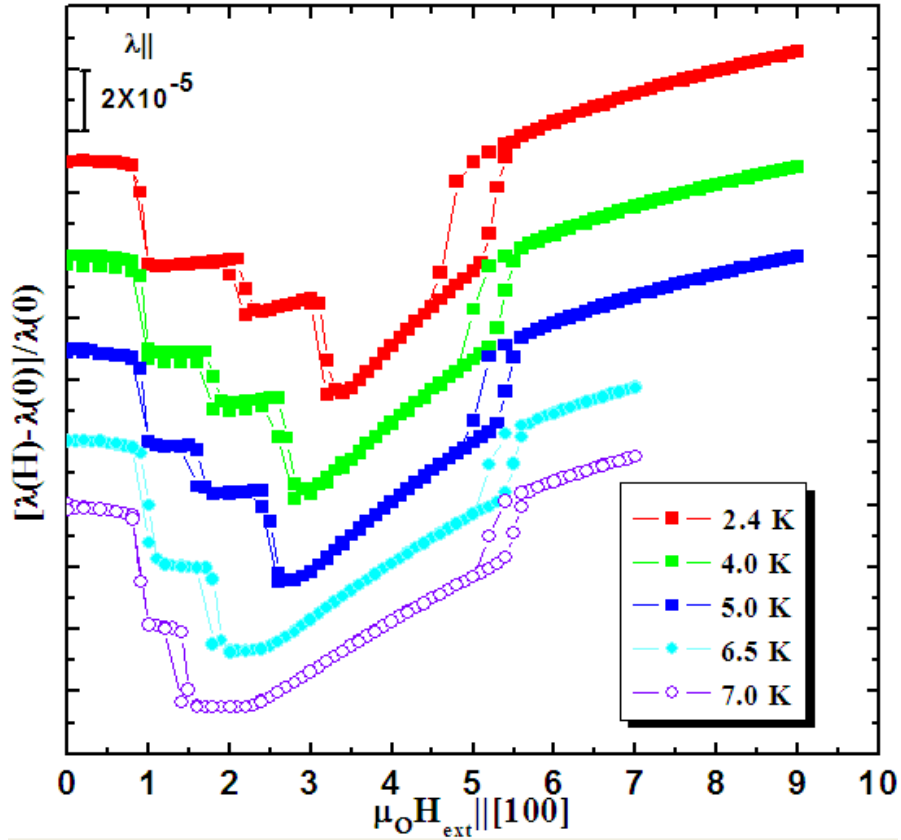


Figure 3.30 The magnetostriction of GdVO₃ single crystal along [100] with magnetic field applied along measured direction at temperatures 2.4, 4, 5, 6.5 7 K.

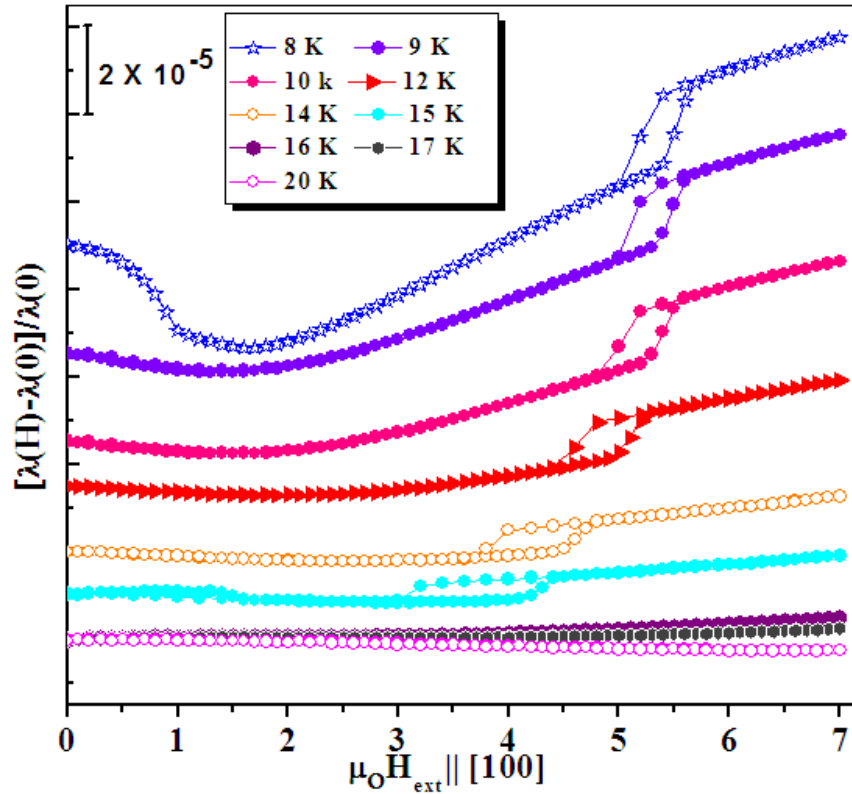


Figure 3.31 The magnetostriction of a GdVO₃ single crystal along [100] with magnetic field applied along measured direction at temperatures 8, 9, and 10,12,14,15,16,17,20 K.

3.3.3 Discussion

The magnetic Phase diagram deduced from the anomalies observed in the magnetostriction (open symbols) and the thermal expansion (filled symbols) measurements along [100] direction is shown in Figure 3.32. Four magnetically ordered states AF2, AF3, AF4 and F have been observed in magnetostriction and thermal expansion measurements. The phase areas are labelled according to those determined by magnetic X-ray scattering. The phase boundaries do not match exactly to those reported for $H \leq 3$ T from magnetic X-ray scattering shown in Figure 3.28.

The first magnetic phase transition at around 0.9 T is observed in the temperature range 2.4 to 7 K, which was also observed in the magnetisation and magnetostriction data [L. D. Tung Private communication]. The third magnetic phase AF3 appeared around 2 T at 2.4 K. This magnetic phase is shifted towards lower field with increasing temperature and at 7 K it appears at a magnetic field of 1.45 T. The transition is

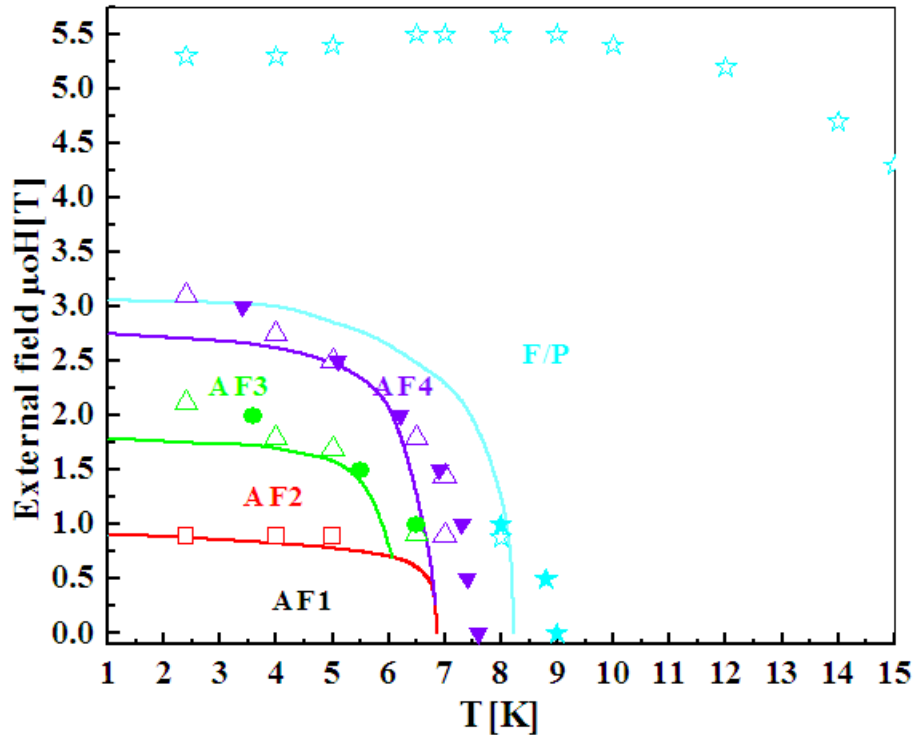


Figure 3.32 Magnetic phase diagram for the Gd magnetism in a GdVO₃ single crystal as derived from magnetostriction (Open symbols) and thermal expansion (Filled symbols) at different magnetic fields. The magnetic field was applied along the [100] direction. The symbols are experimental data, and the lines separating the phases are guide to the eyes and derived from synchrotron data do not match exactly to present data. The measurements were carried out with increasing temperature.

observed in zero field or small field from AF1 to AF4 at 7 K as observed in magnetic X-ray scattering data occurs at 7.7 K in the thermal expansion data. At 9 K the transition into the paramagnetic state is observed, this transition was appeared at 8 K in magnetic X-ray scattering. Thus, the Néel temperature observed in the thermal expansion experiment is 1 K above that seen in the magnetic X-ray scattering data. The transition from AF3 to AF4 occurs in field 0.9 T at 7 K. The AF4 phase exists in 1 K temperature range. The ferromagnetic state (F) reached at ~ 3 T. The positions of the transitions, AF2-AF3, AF3-AF4, and AF4-F observed in magnetostriction and thermal expansion data of present work are not exactly agreement with magnetic X-ray scattering, magnetization and magnetostriction data. The present dilatometer experimental data are measured with two different sensors, which agree with each other so we believe that the temperature is more accurate than in that X-ray diffraction experiment. From the phase diagram a new transition is observed in magnetostriction

at around 5.5 T. This transition was not detected in X-ray magnetic scattering because the previous magnetisation and magnetic X-ray scattering was performed at lower field. Furthermore, this transition has hysteretic behaviour and this transition appeared at around 5 T in decreasing field.

3.3.4 Magnetostriction of GdVO₃ along [110] direction

Figure 3.33 shows the magnetostriction of GdVO₃ along [110] direction with fields applied along [110] direction. The magnetostriction is measured in the temperature range 4 -10 K with magnetic field up to $\mu_0 H = 9$ T. The magnetostriction curves at temperature 4 K to 7 K show the same qualitative behaviour. At 4 K three anomalies indicate transitions at $\mu_0 H = 1.9, 3, 3.5$ T. The third transition disappeared at temperatures 5 K and 6 K but appeared again at 7 K and also transitions slightly shifted towards lower temperature. At temperature $T = 8$ K and higher the magnetostriction becomes negative.

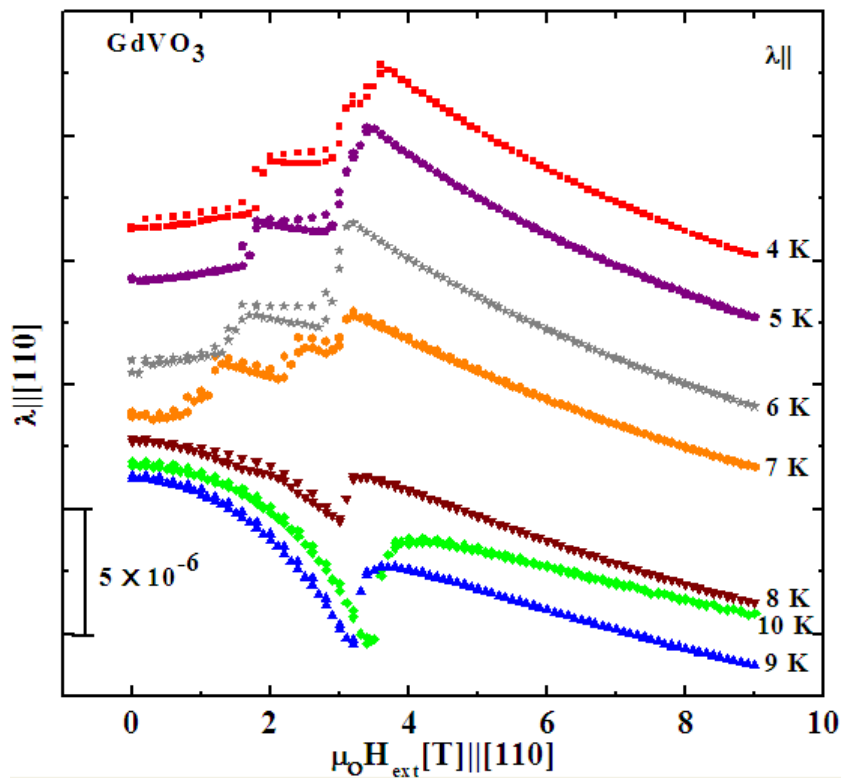


Figure 3.33 Longitudinal magnetostriction of GdVO₃ with field applied along [110] direction.

Conclusions

The magnetostriction and thermal expansion were carried out on polycrystal GdAg_2 magnetic field up to 9 T and temperature range of 2-280 K. When the result of thermal expansion compared with the thermal expansion of single crystal along a-axis from literature by chance, the polycrystalline sample came out as preferential oriented along a-axis, which was later confirmed by X-ray diffraction. We calculated the saturation magnetic field from standard model: the value of the saturation magnetic field is 37 T and found good agreement with experimental value. Moreover, we also confirmed the Néel temperature and transitions in literature. The data indicates some similarities to $\text{GdNi}_2\text{B}_2\text{C}$.

For $\text{PrFe}_4\text{As}_{12}$ the magnetostriction and thermal expansion were measured on single crystal along [100] and [111] direction. The data of zero field thermal expansion and forced magnetostriction along and perpendicular to magnetic field cannot be explained by a random domain distribution so the data are explained through a microscopic model for domain effects.

For GdVO_3 the magnetostriction measurement was performed on single crystal along [100] direction and 110-direction field up to 9 T. Anomalies were observed below 6 T which are also found in literature data but the position of these transitions do not exactly match with literature. We observed a new transition at around 5 T which has not been observed in magnetization and therefore extended the magnetic phase diagram. Further magnetic x-ray scattering experiments are in progress to elucidate the nature of magnetic phases with field applied along [110] and [100].

References

- [1955Bij] D. Bijl and H. Pullan, *Physica Amsterdam* **21**, 285, 1955.
- [1956Boz] R. M. Bozorth, H. J. Williams, and D. E. Walsh, *Phys. Rev.* **103**, 572, 1956.
- [1963Cal] E. Callen, and H.B.Callen, *Phys. Rev.* **129**, 578, 1963.
- [1964Hut] M.T. Hutchings in *Hand book of magnetic materials*, **Vol. 16**, edited by F. Seitz and D. Thurnbull, Academic Press, New York, p. 227,1964.
- [1965Cal] E. Callen and H.B. Callen, *Phys, Rev.* **139**, 55, 1965.
- [1965Cla] A. E.Clark, B.F. DeSavage and R. Bozorth, *Phys. Rev.* **138**, A216, 1965.
- [1967Dwi] A. Dwight, J. Downey, and R. Conner, *Acta Crystallogr.* **22**, 745, 1967.
- [1968Cal] E. Callen, *J. Appl. Phys.* **39**, 519, 1968.
- [1972Whi] G. K. White and J. G. Collins, *J. Low Temp. Phys.* **7**, 43, 1972.
- [1973Bra] G. Brãndli and R. Griessen, *Cryogenics* **13**, 299, 1973.
- 1990Gen] J. Genossar and M. Steinitz, *Rev. Sci. Instrum.* **61**, 2469, 1990.
- [1975Oha] M. Ohashi, T. Kaneko, and S. Miura, *J. Phys. Soc. Jpn.* **38**, 588, 1975.
- [1977 The] Thermo physical Properties of Matter-The TPRC Data Series. IFI/Plenum Data Co., 1977.
- [1977Sak] T. Sakai, G. Adachi, J. Shiokawa, and T. Shin-ike, *J. Appl. Phys.* **48**, 379, 1977.
- [1980Bar] T. H. K. Barron, J. G. Collins, and G. K. White. Thermal expansion of solids at low temperature. *Adv. Phys.* , 29:609, 1980.
- [1980Bru] D. J. Braun and W. Jeitschko, *J. Solid state Chem.* **32**, 357, 1980.
- [1980Cla] A. E.Clark, in *ferromagnetic Materials*, **Vol. 1**, edited by E.P. Wohlfarth, Elsevier, Amsterdam, p. 531,1980.
- [1983Pot] R. Pott and R. Schefzyk, *J. Phys. E.* **16**, 444, 1983.
- [1987Tor] M.s. torikine, et al, *Phys. Rev. B.* **36**, 8660, 1987.
- [1990Mor] P. Morin and D. Schmitt, in *Ferromagnetic Materials*, **Vol. 5**, edited

- by K.H.J. Buschow and E.P. Wohlfarth, Elsevier, Amsterdam, p. 1, 1990.
- [1991Gig] D. Gignoux, P. Morin, and D. Schmitt, *J. Magn. Magn. Mater.* **102**, 33, 1991.
- [1993Gra] E. Gratz, M. Rotter, A. Lindbaum, H. Müller, E. Bauer and H. Kirchmayr, *J. Phys. Cond Mat.* **5**, 567, 1993.
- [1993Gra] E. Gratz, M. Rotter, A. Lindbaum, H. Müller, E. Bauer and H. Kirchmayr, *Materials of Science Forum* **461**, 133-136, 1993.
- [1993Whi] G. K. White, *Thermochim. Acta* **218**, 83, 1993.
- [1994Rot] K. Rottger, A. Endriss, J. Ihringer, S. Doyle and W. F. Kuhs, *Acta Crystallogr., Sect. B*, **50**, 644, 1994.
- [1995Kim] Y. Kimishima, M. Takahashi, K. Okada, H. Ishikawa, and Y. Ichiyonagi, *J. Magn. Magn. Mater.* **140-144**, 1185, 1995.
- [1997Sek] C. Sekine, et al. *Phys. Rev. Lett* **79**, 3218, 1997.
- [1997Shi] I. Shirovani, et al., *Phys. Rev. B*, **567**, 866, 1997.
- [1997Swe] C. A. Swenson, *Rev. Sci. Instrum.* **68**, 1312, 1997.
- [1997The] Thermophysical Properties of Matter-The TPRC Data Series. IFI/Plenum Data Co., 1977.
- [1998Rot] M. Rotter, H. Müller, and E. Gratz, *Rev. Sci. Instrum.*, **69**, 2742, 1998.
- [2000Mat] T. D. Matsuda, et al., *Phys. B* **281-282**, 2000.
- [2000Sat] H. Sato, et al., *Phys. B*. **306**, 281, 2000.
- [2000Tak] N. Takeda, et al., *J. Phys. Soc. Japan*, **69**, 868, 2000.
- [2002Lin] A. Lindbaum and M. Rotter, *Magnetic Materials*, edited by K.H.J. Buschow, Elsevier, Amsterdam, **Vol. 14**, pp. 307–362, 2002
- [2003Miy] S. Miyasaka, Y. Okimoto, M. Iwama, and Y. Tokura, *Phys. Rev. B* **68**, 100406, 2003.
- [2003Mot] Y. Motome, H. Seo, Z. Fang, and N. Nahaosa, *Phys. Rev. Lett.*, **90**, 14602 (2003)
- [2003Mot] Y. Motome, H. Seo, Z. Fang, and N. Nagaosa, *Phys. Rev. Lett.* **90**, 146602, 2003.
- [2003Rot] M. Rotter, M. Loewenhaupt, M. Doerr, A. Lindbaum, H. Sassik, K.

- Ziebeck, B. Beuneu, *Phys. Rev. B* **68**, 144418, 2003.
- [2003Ulr] C. Ulrich, G. Khaliullin, J. Sirker, M. Reehuis, M. Ohl, S. Miyasaka, Y. Tokura, and B. Keimer, *Phys. Rev. Lett.* **91**, 257202 2003.
- [2003Ulr] C. Ulrich, G. Khaliullin, J. Sirker, M. Reehuis, M. Ohl, S. Miyasaka, Y. Tokura, and B. Keimer, *Phys. Rev. Lett.*, **91**, 257202 (2003)
- [2004Miy] S. Miyashita, A. Kawauchi, N. kawakami, and G. khaliullin, *Phys. Rev. B*, **69**, 104425 (2004)
- [2005Doe] M. Doerr, M. Rotter, and A. Lindbaum. *Adv. Phys.*, **54**,1-66, 2005.
- [2005Miy] S. Miyasaka, S. Onada, Y. Okimoto, J. Fujioka, M. Iwama, N. nagaosa, and Y. ToKura, *Phys. Rev. Lett.*, **94**, 076405 (2005)
- [2005Tun] L. D. Tung, *Phys. Rev. B* **72**, 054414, 2005.
- [2006Bar] Alexander Barcza, Diploma Thesis. Magnetostriction in rare Earth Elements Measured with Capacitance Dilatometry, 2006.
- [2006Rot] M. Rotter, A. Lindbaum, A. Barcza, M. El Massalami, M. Doerr, M. Loewenhaupt, H. Michor, B. Beuneu, *Europhys Lett* **75 (1)**, 160, 2006.
- [2006Tun] L. D. Tung, *Phys. Rev. B*, **73**, 024428 (2006)
- [2007Rot] M. Rotter, M. Doerr, M. Zschintzsch, A. Lindbaum, H.Sassik, G. Behr *J. Magn. Magn. Mater* **310**, 1383-1385,2007
- [2007Tun] L. D. Tung, M.R. Lees, G. Balakrishnan, *Phys. Rev. B*, **75**, 104404 (2007)
- [2008Hen] Z. Henkie et al. *J. Phys. Soc. Jpn.* **77**, 128–134, 2008.
- [2008Say] T. A. Sayles, W.M.Yuhasz, J. Paglione, T. Yanagisawa, J.R. Jeffries, M.B. Maple, Z. Henkie, A. Pietraszko, T. Cichorek, R. Wawryk, Y. Nemoto, T. Goto, *Physica B*, **403**, 869, 2008.
- [2008Jen] Jens Jensen, Martin Rotter , *Physical review B*, **77**, 134408 (2008)